

# Stellar atmosphere parameters with MA $\chi$ , a MAssive compression of $\chi^2$ for spectral fitting

P. Jofré<sup>1</sup>, B. Panter<sup>2</sup>, C. J. Hansen<sup>3</sup>, and A. Weiss<sup>1</sup>

<sup>1</sup> Max-Planck-Institut für Astrophysik, Karl-Schwarzschild-Str. 1, 85741 Garching, Germany  
e-mail: jofre@mpa-garching.mpg.de

<sup>2</sup> Institute for Astronomy, University of Edinburgh, Royal Observatory, Blackford Hill, Edinburgh EH9 3HJ

<sup>3</sup> European South Observatory (ESO), Karl-Schwarzschild-Str. 2, 85748 Garching, Germany

## ABSTRACT

MA $\chi$  is a new tool to estimate parameters from stellar spectra. It is based on the maximum likelihood method, with the likelihood compressed such that the information stored in the spectral fluxes is conserved. The compressed data is given by the size of the number of parameters, rather than the number of flux points. The optimum speed up enabled by the compression is the ratio of the data set to the number of parameters. The method has been tested using a sample of low resolution spectra from the Sloan Extension for Galactic Understanding and Exploration (SEGUE) survey in the estimation of metallicity, effective temperature and surface gravity, with accuracies of 0.24 dex, 130K and 0.5 dex, respectively. A comparison of the stellar parameters with those recovered by the SEGUE Stellar Parameter Pipeline give a reasonable agreement. A small sample of high resolution VLT-UVES spectra is also used to test the method against a more classical approach. The speed and multi-resolution capability of MA $\chi$ , combined with its performance against other methods, indicates that it will be a useful tool for the analysis of upcoming spectral surveys.

**Key words.** Techniques: spectroscopic - Surveys - Stars: fundamental parameters

## 1. Introduction

The astronomical community has conducted many massive surveys of the Universe, and many more are either ongoing or planned. Recently completed is the Sloan Digital Sky Survey (SDSS, York et al. 2000), notable for assembling in a consistent manner the positions, photometry and spectra of millions of galaxies, quasars and stars, and covering a significant fraction of the sky. The size of such a survey allows to answer many questions about the structure and evolution of our universe. More locally, massive surveys of stars to reveal their properties have been undertaken, for example the Geneva-Copenhagen Survey for the Solar neighborhood (Nordström et al. 2004) and the ELODIE library (Prugniel et al. 2007). These surveys provide a large amount of stellar photometry and spectra from the solar neighborhood, broadening the range of stellar types studied. SEGUE – Sloan Extension for Galactic Understanding and Exploration (Yanny et al. 2009) – a component of SDSS, contains additional imaging data at lower galactic latitudes, in order to better explore the interface between the disk and halo population.

By analyzing statistically the properties of these stars, such as chemical abundances, velocities, distances, etc, it has been possible to match the structure and evolution of the Milky Way to the current generation of galaxy formation models (Jurić et al. 2008; Ivezić et al. 2008; Bond et al. 2009; Wyse 2006).

Studies of large samples of stars of our galaxy are crucial tests for the theory of the structure and formation of spiral galaxies. Even though the statistics given by SEGUE or the Geneva-Copenhagen survey agree with the models and simulations of galaxy formation, there is some contention over whether the ac-

curacies of measurements adequately support the conclusions. New surveys such as RAVE (Steinmetz et al. 2006) and Gaia (Perryman et al. 2001) will give extremely high accuracies in velocities and positions, LAMOST (Zhao et al. 2006) and part of the SDSS-III project, APOGEE and SEGUE-2 (Rockosi et al. 2009), will give high quality spectra and therefore stellar parameters and chemical abundances of millions of stars over all the sky. These more accurate properties and larger samples should increase our knowledge of the Milky Way and answer wider questions about the formation and evolution of spiral galaxies. As data sets grow it becomes of prime importance to create efficient and automatic tools capable of producing robust results in a timely manner. A standard technique for estimating parameters from data is the maximum likelihood method. In a survey such as SEGUE, which contains more than 240,000 stellar spectra, each with more than 3000 flux measurements, it becomes extremely time consuming to do spectral fitting using a brute-force search on the multi-dimensional likelihood surface, even more so, if one wants to explore the errors on the recovered parameters.

Efforts to reduce the computational burden of characterizing the likelihood surface include Markov Chain Monte Carlo methods (Ballot et al. 2006), where a chain is allowed to explore the likelihood surface in order to determine the global solution. An alternative method is to start at an initial estimate and hope that the likelihood surface is smooth enough that a gradient search will converge on the solution. An example of this approach can be found in Allende Prieto et al. (2006) and Gray et al. (2001), based on the Nelder-Mead downhill simplex method (Nelder & Mead 1965), where the derivatives of the likelihood function give the direction toward the maximum. In both cases, the likelihood is evaluated only partially, leaving large amounts of parameter space untouched. Moreover, the time needed to find

the maximum depends on the starting point and the steps used to evaluate the next point.

Another parameter estimation method utilizes neural networks, for example Snider et al. (2001) and Re Fiorentin et al. (2007). While these non-linear regression models can obtain quick accurate results, they are entirely dependent on the quality of the training data, in which many parameters must be previously known. Careful attention must also be paid to the sampling of the model grid which is used to generate the neural network.

An alternative approach to spectral analysis is the Massively Optimized Parameter Estimation and Data compression method (MOPED<sup>1</sup>, Heavens et al. 2000). This novel approach to the maximum likelihood problem involves compressing both data and models to allow very rapid evaluation of a set of parameters. The evaluation is fast enough to do a complete search of the parameter space on a finely resolved grid of parameters. Using carefully constructed linear combinations, the data is weighted and the size is reduced from a full spectrum to just one number per parameter. This number, with certain caveats (discussed later), encapsulates all the information about the parameter contained in the full data. The method has been successfully applied in the fields of CMB analysis (Bond et al. 1998), medical image registration<sup>2</sup> and galaxy shape fitting (Tojeiro et al. 2007). A complete background of the development of the MOPED algorithm can be found in Tegmark et al. (1997, hereafter T97), Heavens et al. (2000, hereafter H00) and Panter et al. (2003).

In this article we present a new derivative of MOPED, MA $\chi$  (MASSive compression of  $\chi^2$ ), to analyse stellar spectra. To estimate, for example, the metallicity history of a galaxy, MOPED needs models where the spectra are the sum of single stellar populations. Here we want to study one population, meaning the metallicity has to be estimated from the spectrum of each single star. It is therefore necessary to develop a specific tool for this task: MA $\chi$ . In Sect. 2 we describe the method, giving a summary of the derivation of the algorithm. We then test the method in Sect. 3 on the basic stellar atmosphere parameters estimation of a sample of low resolution stars of SEGUE, where we compare our results with the SEGUE Stellar Parameter Pipeline in Sect. 4 and finally check the method for a small sample of high resolution spectra in Sect. 5, where we compare our results with a more classical approach for a small sample of VLT-UVES spectra. A summary of our conclusions is given in Sect. 6.

## 2. Method

In this section we describe our method to treat the likelihood surface. We first review the classical maximum likelihood method, where a parametric model is used to describe a set of data. Second, we present the algorithm that compresses the data and hence speeds the likelihood estimation. Finally we show the proof for the lossless nature of the compression procedure.

### 2.1. Maximum likelihood description

Suppose the data (e.g. the flux of a spectrum) are represented by  $N$  real numbers  $x_1, x_2, \dots, x_N$ , which are arranged in an  $N$ -dimensional vector  $\mathbf{X}$ . They are the flux measurements at  $N$  wavelength points. Assume that each data point  $x_i$  has a signal part  $\mu_i$  and a noise contribution  $\sigma_i$ :

$$x_i = \mu_i + \sigma_i \quad (1)$$

<sup>1</sup> MOPED is protected by US Patent 6,433,710, owned by The University Court of the University of Edinburgh (GB)

<sup>2</sup> <http://www.blackfordanalysis.com>

If the noise has zero mean,  $\langle \mathbf{X} \rangle = \langle \boldsymbol{\mu} \rangle$ , we can think of  $\mathbf{X}$  as a random variable of probability distribution  $L(\mathbf{X}, \boldsymbol{\Theta})$ , which depends in a known way on a vector  $\boldsymbol{\Theta}$  of  $m$  model parameters. In the present case  $m = 3$  with

$$\boldsymbol{\Theta} = (\theta_1, \theta_2, \theta_3) = ([\text{Fe}/\text{H}], T_{\text{eff}}, \log g) \quad (2)$$

with the iron abundance  $[\text{Fe}/\text{H}]$ , effective temperature  $T_{\text{eff}}$  and surface gravity  $\log g$ . A certain combination of the single parameters  $\theta_j$  ( $j = 1, 2, 3$ ), also produces a theoretical model,  $\mathbf{F} = \mathbf{F}(\boldsymbol{\Theta})$  and we can build an  $m$ -dimensional grid of theoretical models by varying the  $\theta_j$  parameters. If the noise is Gaussian and the parameters have uniform priors, then the likelihood

$$L_f(\mathbf{X}, \boldsymbol{\Theta}) = \frac{1}{(2\pi)^{N/2} \sqrt{\sigma_{\text{av}}^2}} \exp \frac{-\chi^2}{2} \quad (3)$$

gives the probability for the parameters, where  $\sigma_{\text{av}}^2$  is the averaged square of the noise of each data point and

$$\chi^2 = \sum_{i=0}^N \frac{(F_i - \mu_i)^2}{\sigma_i^2}. \quad (4)$$

The position of its maximum estimates the set of parameters  $\boldsymbol{\Theta}_0$  that best describe the data  $\mathbf{X}$ . The fit between  $\mathbf{F}(\boldsymbol{\Theta}_0)$  and  $\mathbf{X}$  is good if  $\chi^2 < \text{DOF}$ , where  $\text{DOF} = N - m$  are the degrees of freedom. In the most basic form one finds the maximum in the likelihood surface by exploring all points in parameter space, with each likelihood estimation calculated using all  $N$  data points. This procedure is, of course, very time-consuming if  $N$  and  $m$  are large.

### 2.2. Data compression

In practice not all data points give information about the parameters, because either they are noisy or not sensitive to the parameter under study. The MOPED algorithm uses this knowledge to construct weighting vectors which neglect some data without losing information. A way to do this is by forming linear combinations of the data.

Let us compress the information of a given parameter  $\theta_j$  from our spectrum. The idea is to capture as much as possible information about this particular parameter. We define our weighting vector  $\mathbf{b}_j = (b_{j,1}, b_{j,2}, \dots, b_{j,N})$  as

$$\mathbf{b}_j = \frac{1}{|\mathbf{b}_j|} \frac{1}{\sigma^2} \frac{\partial \mathbf{F}}{\partial \theta_j} \quad (5)$$

where  $|\mathbf{b}_j| = \sqrt{\mathbf{b}_j \cdot \mathbf{b}_j}$ . This definition assures that each data point of the spectrum is less weighted if  $\sigma$  is large and more weighted if the sensitivity in the flux – meaning the derivative of  $\mathbf{F}$  respect to the parameter  $\theta_j$  – is large. To create this vector we need, on one hand, the information about the behavior of the parameters from a theoretical fiducial model, and on the other hand, the error measurement from the data.

Figure 1 shows the example of the weighting vectors for the parameters of the set (2) using a fiducial model with  $[\text{Fe}/\text{H}] = -2.0$ ,  $T_{\text{eff}} = 6000$  K and  $\log g = 4.0$ . The upper panel corresponds to the synthetic spectrum at the SDSS resolving power ( $R = 2000$ ) and the panels B, C and D to the weighting vector for metallicity, effective temperature and surface gravity, respectively. This figure is a graphical representation of Eq. (5), and helps to visualize better the weight in relevant regions of the spectrum.

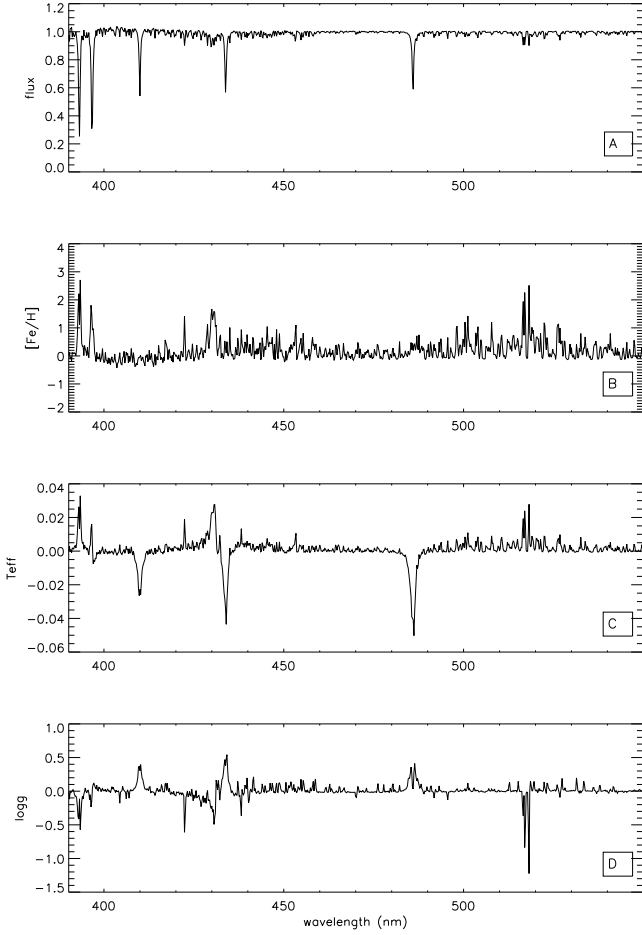


**Fig. 1.** (A) Fiducial model with parameters  $[\text{Fe}/\text{H}] = -2.0$ ,  $T_{\text{eff}} = 6000$  K and  $\log g = 4.0$ . Other panels indicate the weighting vectors according to Eq. (5) for metallicity (B), temperature (C) and surface gravity (D).

In the case of metallicity (panel B), the major weight is concentrated in the 2 peaks at 3933 and 3962 Å, corresponding to the CaII K and H lines seen in the synthetic spectrum at panel A. The second important region with weights is close to 5180 Å, corresponding to the MgIb triplet. A minor peak is seen at 4300 Å, which is the G-band of the CH molecule. These 3 features are metallic lines, therefore show a larger dependency on metallicity than the rest of the vector, which is dominated by a zero main weight.

For the temperature (panel C) the greatest weight is focused on the hydrogen Balmer lines at 4101, 4340 and 4861 Å. Peaks at the previous metallic lines are also seen, but with a minor amplitude. Finally, the surface gravity (panel D) presents the strongest dependency on the MgI triplet. The wings of the CaII and Balmer lines also present small dependencies. As in the case for metallicity, the rest of the continuum is weighted by a close to zero mean.

The weighting is done by multiplying these vectors with the spectrum, where the information kept from the spectrum is given by the peaks of the weighting vector. We define this procedure as “compression”, where the information about the parameter  $\theta_j$  is expressed as

$$y_{j,\mathbf{X}} = \mathbf{b}_j \cdot \mathbf{X}, \quad j = 1, 2, 3 \quad (6)$$

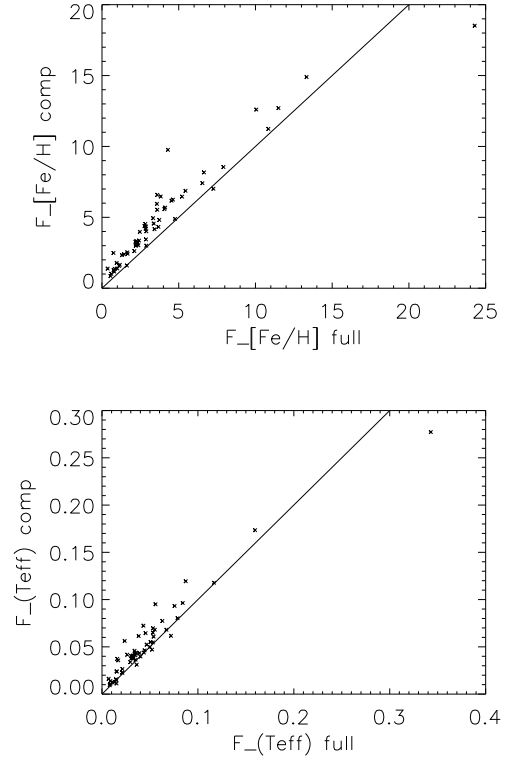


**Fig. 2.** Correlations between the Fisher matrix values obtained from the full and compressed likelihoods for metallicity (upper panel) and effective temperature (lower panel) for 75 randomly selected stars of SEGUE. The line corresponds to the one-to-one relation.

with  $\mathbf{X}$  the spectrum. With the weighting vector defined in Eq. (5) we can compress data ( $\mathbf{X}$ ) and model ( $\mathbf{F}$ ) by using Eq. (6). Since  $\mathbf{b}_j$  and  $\mathbf{X}$  (or  $\mathbf{F}$ ) are  $N$ -dimensional, the product  $y_j$  in (6) is a number, which stores the information about the parameter  $\theta_j$ .

In order to perform a compression for all the parameters simultaneously, we require that  $y_k$  is uncorrelated with  $y_j$ , with  $j \neq k$ . This means that the  $\mathbf{b}$ -vectors must be orthogonal, i.e.  $\mathbf{b}_k \cdot \mathbf{b}_j = 0$ . Following the procedure of H00 we find the other  $y_k = \mathbf{b}_k \cdot \mathbf{X}$  by Gram-Schmidt orthogonalization:

$$\mathbf{b}_k = \frac{1}{|\mathbf{b}_k|} \left[ \frac{1}{\sigma^2} \frac{\partial \mathbf{F}}{\partial \theta_k} - \sum_{q=1}^{m-1} \left( \frac{\partial \mathbf{F}}{\partial \theta_k} \cdot \mathbf{b}_q \right) \mathbf{b}_q \right] \quad (7)$$

For  $m = 3$  we have the numbers  $y_{1,\mathbf{X}}, y_{2,\mathbf{X}}, y_{3,\mathbf{X}}$ , for the data and  $y_{1,\mathbf{F}}, y_{2,\mathbf{F}}, y_{3,\mathbf{F}}$  for the models, corresponding to the parameters of  $\Theta$  given in Eq. (2)

#### Goodness of fit

The definition of  $\chi^2$ , which is the sum of the differences of the data and the model, motivates us to define our goodness of fit. The “compressed”  $\chi_c^2$  is the sum of the differences of the compressed data and model:

$$\chi_{c,\theta_j}^2 = \frac{1}{\sigma_{\text{av}}^2} (y_{j,\mathbf{X}} - y_{j,\mathbf{F}})^2 \quad (8)$$

which gives the probability for the parameter  $\theta_j$

$$L_{c,j}(\mathbf{X}, \theta_j) = \frac{1}{(2\pi)^{N/2} \sqrt{\sigma_{av}^2}} \exp \frac{-\chi_{c,\theta_j}^2}{2} \quad (9)$$

Since the  $y_j$  numbers are by construction uncorrelated, the ‘‘compressed’’ likelihood of the parameters is obtained by multiplication of the likelihood of each single parameter  $L_{c,j}(\mathbf{X}, \theta_j)$ :

$$L_c(\mathbf{X}, \Theta) = \prod_{j=1}^m L_{c,j}(\mathbf{X}, \theta_j) = \frac{1}{((2\pi)^{N/2} \sqrt{\sigma_{av}^2})^m} \exp \frac{-\chi_c^2}{2} \quad (10)$$

where

$$\chi_c^2 = \frac{1}{\sigma_{av}^2} \sum_{j=0}^m (y_{j,\mathbf{X}} - y_{j,F})^2 \quad (11)$$

is the compressed  $\chi^2$ .

As in the classical approach, the peak of the compressed likelihood estimates the parameters  $\Theta_0$  that generate the model  $\mathbf{F}(\Theta_0)$ , which reproduces best the data  $\mathbf{X}$ . The advantage of using the compressed likelihood is that it is fast since the calculation of  $\chi_c^2$  needs only  $m$  iterations and not  $N$  as in the usual  $\chi^2$  computation. The search of the maximum point in the likelihood is therefore done in an  $m$ -dimensional grid of  $y$ -numbers and not of  $N$ -length fluxes.

### 2.3. No loss of information by the compression

The Fisher Information Matrix describes the behavior of the likelihood close to the maximum. Here we use it only to show the lossless compression offered by the MOPED method but a more extensive study is given in T97 and H00.

To understand how well the compressed data constrains a solution we consider the behavior of the logarithm of the likelihood  $L$  near the peak. In the following, we denote a generic  $L$  that can correspond to the compressed likelihood  $L_c$  or the full one  $L_f$ , since the procedure is the same. In the Taylor expansion the first derivatives  $\partial(\ln L)/\partial\theta_j$  vanish at the peak and the behavior around it is dominated by the quadratic terms:

$$\ln L = \ln L_{\text{peak}} + \frac{1}{2} \frac{\partial^2 \ln L}{\partial\theta_j \partial\theta_k} \Big|_{\text{peak}} \Delta\theta_j \Delta\theta_k \quad (12)$$

The likelihood function is approximately a Gaussian near the peak and the second derivatives, which are the components of the inverse of the Fisher Matrix  $\mathcal{F}_{jk}$ , measure the curvature of the peak. Since the dependencies of the parameters are not correlated, the matrix is diagonal with values

$$\mathcal{F}_{jj} = - \frac{\partial^2 \ln L}{\partial\theta_j^2} \quad (13)$$

In Fig. 2 we have plotted the values  $\mathcal{F}_{[\text{Fe}/\text{H}]}$  and  $\mathcal{F}_{T_{\text{eff}}}$ , corresponding to parameters metallicity and effective temperature, respectively, for likelihoods of 75 randomly selected stars of SEGUE, using the classical (full) and the compressed (comp) dataset. The line corresponds to a one-to-one relation. The values correlate well, as expected.

Figure 3 shows full and compressed likelihood surfaces of metallicity and temperature for 4 randomly selected stars, where 8 equally spaced contour levels have been plotted in each case. This is another way to visualize the statement that the Fisher

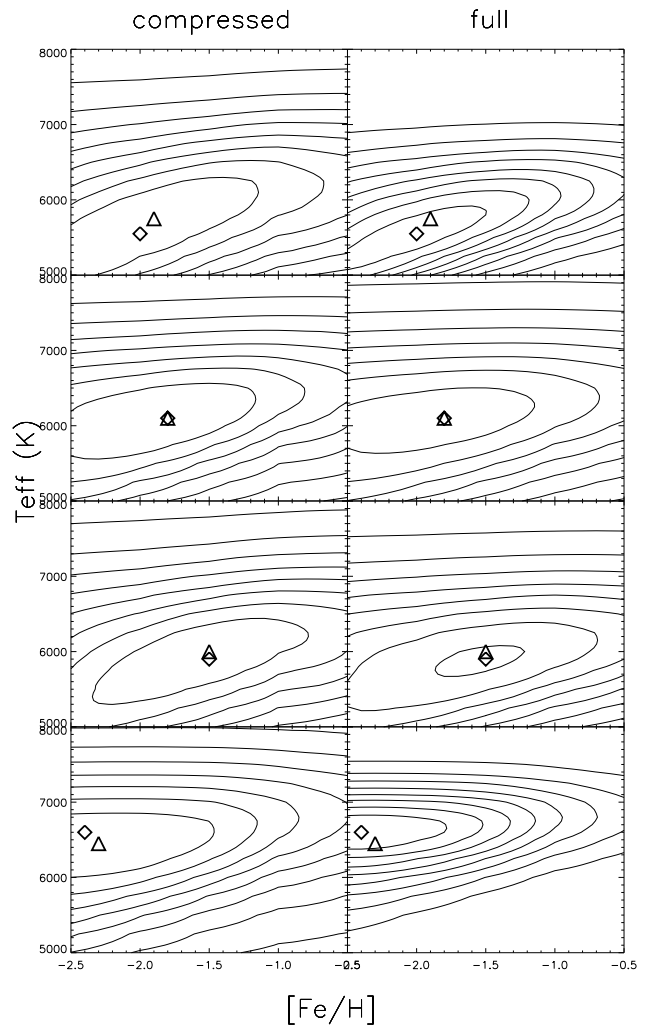


**Fig. 3.** Likelihoods of the compressed data set (left) and full data set (right) in the parameter space of effective temperature and metallicity for 4 randomly selected SEGUE stars. In each panel 8 equally spaced contour levels are plotted. The triangle and diamond correspond to the maximum point of the compressed and the full data set, respectively. Both maxima lie in the first confidence contour level, meaning that both data sets reach the same solution for these two parameters.

Matrices correlate. The curvature of both likelihoods is the same close to the peak, as predicted. In Fig. 3 we have also over-plotted the maximum point of the compressed likelihood as a triangle and the maximum point of the full one as a diamond. It can be seen that the maximum points of the compressed and full data set lie inside the first contour level of the likelihoods. This shows that the compressed data set gives the same solution as the full one - even after the dramatic compression.

In the following parts of the paper the numerical values of  $\chi^2$  correspond to the classical reduced  $\chi^2$ .

### 3. Implementation on Low Resolution Spectra

The sample of stars used to test the method are F-G dwarf stars. Based on the metallicity given by the SEGUE Stellar Parameter Pipeline, we chose metal-poor stars as will be explained below.

This choice allows us to avoid the problem of the saturation of metallic lines such as CaII K (Beers et al. 1999), which is a very strong spectral feature that serves as a metallicity indicator in the low resolution spectra from SEGUE. These stars fall in the temperature range where Balmer lines are sensitive to temperature and the spectral lines are not affected by molecules (Gray 1992). With these considerations, it is correct to assume that the spectra will behave similar under changes of metallicity, temperature and gravity. This allows the choice of a random fiducial model from our grid of models for the creation of the weighting vectors, which will represent well the dependencies of the parameters in all the stars.

### 3.1. Data

We have used a sample of SEGUE stellar spectra (Yanny et al. 2009), part of the Seventh Data Release (DR7, Abazajian et al. 2009) of SDSS. The survey was performed using the 2.5-meter telescope at the Apache Point Observatory in southern New Mexico and contains spectra of  $\sim 240,000$  stars. All the spectra have *ugriz* photometry (Fukugita et al. 1996). From a color-color diagram we identify the dwarf stars and we select them using the sqlLoader (Thakar et al. 2004) under the constraints that the object must be a star and have colors of  $0.65 < u - g < 1.15$  and  $0.05 < g - r < 0.55$ . We verify the spectral type by downloading also the values 'seguetargetclass' and 'hammerstype', which classify our stars mainly as F-G dwarfs. We also constrain the metallicity to be in the range of  $-999 < [\text{Fe}/\text{H}] < -0.5$ . The latter values were taken from the new SEGUE Stellar Parameter Pipeline (Lee et al. 2008a,b; Allende Prieto et al. 2008), where the -999 indicates that the Pipeline has not estimated the metallicity of this particular star.

Our final sample contains spectra of 17,274 stars with a resolving power of  $R \approx 2000$  and a signal-to-noise up to 10. The wavelength range is 3800 – 9200Å and the spectra are with absolute flux.

### 3.2. Grid of Models

The synthetic spectra are created using the synthesis code SPECTRUM (Gray & Corbally 1994), which uses the new fully blanketed stellar atmosphere models of Kurucz (1992) and computes the emergent stellar spectrum under the assumption of local thermal equilibrium (LTE). The stellar atmosphere models assume the solar abundances of Grevesse & Sauval (1998) and plane parallel line blanketed model structure in one dimension. For the creation of the synthetic spectra, we set a microturbulence velocity of 2 km/s, based on the atmosphere model value. The line list file and atomic data were taken directly from the SPECTRUM webpage<sup>3</sup>. In these files, the lines were taken from the NIST Atomic Spectra Database<sup>4</sup> and the Kurucz website<sup>5</sup>. No molecular opacity was considered in the model generation.

We created an initial three dimensional grid of synthetic spectra starting from the ATLAS9 Grid of stellar atmosphere models of Castelli & Kurucz (2003) by varying the parameters  $\Theta$  of Eq. (2). They cover a wavelength range from 3800 to 7000 Å in steps of  $\Delta\lambda = 1\text{Å}$ , based on the wavelength range of SDSS spectra together with our line list. This wavelength range is large enough for a proper continuum subtraction, as described in Sect. 3.3. The spectra have an absolute flux and are finally

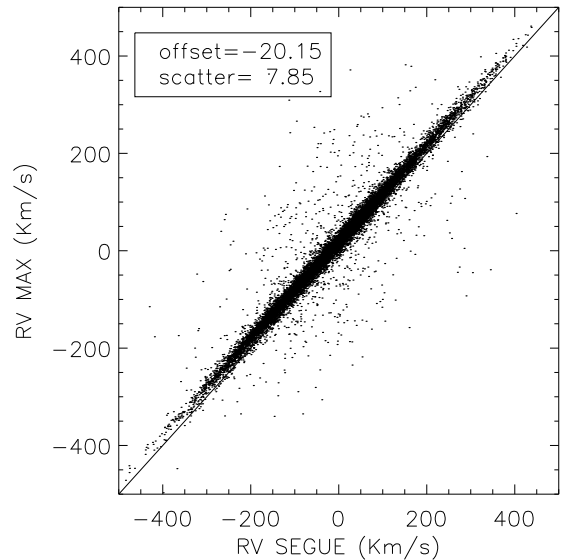


**Fig. 4.** Radial velocities found using minimum fluxes of strong lines given by Table 1 (MAX) against those of the SEGUE database. The difference of the radial velocities given by the SEGUE database with those obtained by our method is indicated in the legend as offset, with its standard deviation as scatter.

smoothed to a resolving power of  $R = 2000$ , according to SDSS resolution.

In order to have a finer grid of models, we interpolated linearly the fluxes created for the initial grid. It has models with  $-2.5 \leq [\text{Fe}/\text{H}] \leq -0.5$  with  $\Delta[\text{Fe}/\text{H}] = 0.1$  dex,  $5000 \leq T_{\text{eff}} \leq 8000$  with  $\Delta T_{\text{eff}} = 50$  K and  $3.5 \leq \log g \leq 5$  with  $\Delta \log g = 0.1$  dex. The scaling factor for the normalization varies linearly from 0.85 to 1.15 in steps of 0.01 (see below). Our final grid has  $21 \times 61 \times 16 \times 30 = 614,880$  models. We set a linearly varying  $[\alpha/\text{Fe}]$  of  $[\alpha/\text{Fe}] = [0.2, 0.4]$  for stars in the metallicity range of  $-0.5 \geq [\text{Fe}/\text{H}] \geq -1.0$  and  $[\alpha/\text{Fe}] = 0.4$  for stars with  $[\text{Fe}/\text{H}] \leq -1.0$ , to reproduce the abundance of  $\alpha$  elements in the Milky Way, as in Lee et al. (2008a). This varying  $[\alpha/\text{Fe}]$  abundances also were calculated with interpolation of fluxes created from solar and  $\alpha$ -enhanced ( $[\alpha/\text{Fe}] = 0.4$ ) stellar atmosphere models. We do not include the  $\alpha$  abundances as a free parameter, since we want to estimate the metallicity from lines of  $\alpha$  elements (Ca, Mg) and we would obtain a degeneracy in both parameters. We prefer to create a grid where the  $\alpha$  abundances are already 'known'.

The grid steps between the parameters are smaller than the accuracies expected from the low resolution SEGUE data. The extra time required to calculate the compressed likelihood in this finer grid is not significant, and retaining the larger size allows us to demonstrate the suitability of the method for future, more accurate data capable of using the full grid.

### 3.3. Matching models to data

Data and model need to be prepared for the analysis. First of all, the data must be corrected from vacuum wavelength frame of the observations to the air wavelength frame of the laboratory. Secondly, we must correct for the Doppler effect  $z_c$ . This is done by using the flux minimum of the lines indicated in Table 1 except the MgI b triplet, since this feature is not seen clear enough

<sup>3</sup> <http://www1.appstate.edu/dept/physics/spectrum/spectrum.html>

<sup>4</sup> <http://physics.nist.gov/PhysRefData/ASD/index.html>

<sup>5</sup> <http://kurucz.harvard.edu/linelists.html>

**Table 1.** Strongest lines in F-G dwarf stars. First column indicates the name of the line and the second its wavelength position in Å.

line	$\lambda$ Å
Ca <i>IK</i>	3933
Ca <i>IH</i>	3962
H $\delta$	4101
H $\gamma$	4340
H $\beta$	4861
Mg b triplet	5183

in every spectra, driving in our automatic  $z\epsilon$  calculation to unrealistic values. A comparison of the radial velocity found with this method with the value given by the SEGUE database is shown in Fig. 4. The difference of the radial velocities (SEGUE - MAX) has an mean (offset) of -20.15 km/s with standard deviation (scatter) of 7.85 km/s. The effect of this difference in the final parameter estimation is discussed in Sect.4. Once our data is corrected by Doppler effect, they must be interpolated to the wavelength points of the models, in order to have the same data points.

For automatic fitting of a large sample of stars using a large grid of models, we decided to normalize the flux to a fitted continuum. In this way the dependency of the parameters is concentrated mainly on the line profiles. The choice of the normalization method is a difficult task, since none of them is perfect. It becomes especially difficult in regions where the spectrum shows too many strong absorption features, as the CaII lines of Table 1. Using the same method for models and data, difficult regions behave similar in both cases, allowing a final fitting in these complicated regions as well. We have adopted the normalization method of Allende Prieto et. al. (2006), because it works well for the large spectral range of SDSS spectra. It is based on an iteratively polynomial fitting of the pseudo-continuum, considering only the points that lie inside the range of  $4\sigma$  above and  $0.5\sigma$  below. Then we divide the absolute flux by the final pseudo-continuum. Due to noise, the continuum of the final flux may not necessary be at unity. We include a new degree of freedom in the analysis that scales this subtracted continuum. This scaling factor for the normalization is then another free parameter, having finally 4 parameters to estimate – 3 stellar atmosphere parameters and the scaling factor. The final step is to choose the spectral range for the analysis.

### 3.4. Compression Procedure

We chose the fiducial model with parameters  $[\text{Fe}/\text{H}] = -2.0$ ,  $T_{\text{eff}} = 6000$  K,  $\log g = 4.0$  and  $a_s = 1$ , to calculate the weighting vectors,  $\mathbf{b}_{[\text{Fe}/\text{H}]}$ ,  $\mathbf{b}_{T_{\text{eff}}}$ ,  $\mathbf{b}_{\log g}$  and  $\mathbf{b}_{a_s}$ , corresponding to metallicity, effective temperature, gravity and scaling factor for normalization, respectively. Next, we calculate the set of  $y$ -numbers using Eq. (6) for each point in the grid of synthetic spectra by projecting the  $\mathbf{b}$ -vectors onto the spectrum, resulting in a four dimensional  $y$ -grid, with every point a single number. With the respective  $\mathbf{b}$ -vectors we calculate the  $y$ -numbers for the observed spectra, the expression (11) for every point in the grid and finally, we find the minimum value in the grid which corresponds to the maximum point of the compressed likelihood.

To refine our solution we find the “real” minimum  $\chi^2$  with a quadratic interpolation. For the errors, we look at the models within the confidence contour of  $\chi^2 = \chi^2_{\text{min}} + \Delta\chi^2$  with  $\Delta\chi^2 =$

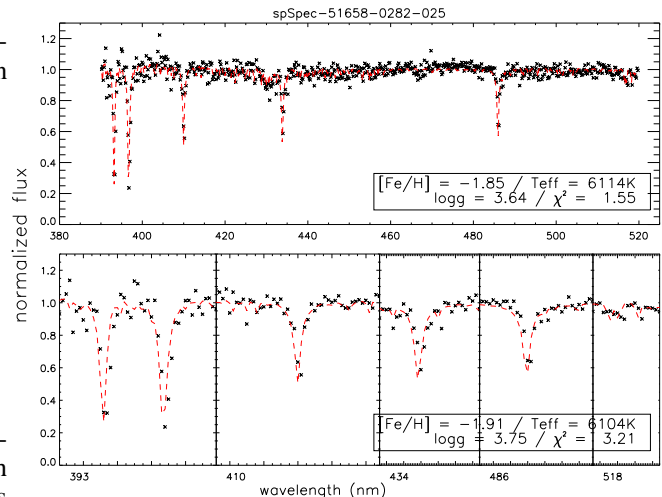


**Fig. 5.** Example of the fit between a randomly selected SEGUE star (crosses) and a synthetic spectrum (red dashed line). The legend indicates the stellar atmosphere parameters of the model and the value of the reduced  $\chi^2$  of the fit. The upper panel is the fit using all the points of the spectral region [3850,5200] Å. The lower panel is the fit using only the data points where the lines of Table 1 are located.

4.72 corresponding to the  $1\sigma$  error in a likelihood with 4 free parameters (for further details see chapter 14 of Press 1993).

## 4. Application to SEGUE spectra

We have chosen to use the wavelength range of [3850,5200] Å, as information about metallicity, temperature and gravity, which is available in the lines listed in Table 1. These spectral lines are strong in F-G stars meaning they can be identified at low resolution without difficulty. The wings of Balmer lines are sensitive to temperature and the wings of strong Mg lines are sensitive to gravity (Fuhrmann 1998). Since iron lines are not strong enough to be distinguished from the noise of our spectra, the CaII K and MgIb lines are our indicators of metallicity (Beers et al. 2000; Allende Prieto et. al. 2006; Lee et al. 2008a).

It is important to discuss the presence of the carbon feature known as the G-band at 4304 Å in our spectral window. The fraction of Carbon-Enhanced Metal-Poor (CEMP) stars is expected to increase with decreasing metallicity (Beers et al. 1992), to about 20% at below  $[\text{Fe}/\text{H}] = -2.0$  (Lucatello et al. 2006), implying possibly a strong carbon feature in the observed spectrum. As discussed by Marsteller et al. (2009), a strong G-band may also affect the measurement of the continuum at the CaII lines, which could result in an underestimation of the stellar metallicity. We commented in Sect. 2 the influence of the lines in the weighting vectors used for the compression and we saw that the G-band also displays minor peaks (see Fig. 1). The role of this minor dependency in comparison with those from the CaII, Balmer and MgI lines can be studied by comparing the final parameter estimation when using the whole spectral range or only the regions with the lines of Table 1, where the G-band is not considered. A further motivation of performing an analysis of entire range against spectral windows is also explained in the following. The implications of this tests in terms of fraction of CEMP stars is discussed below.

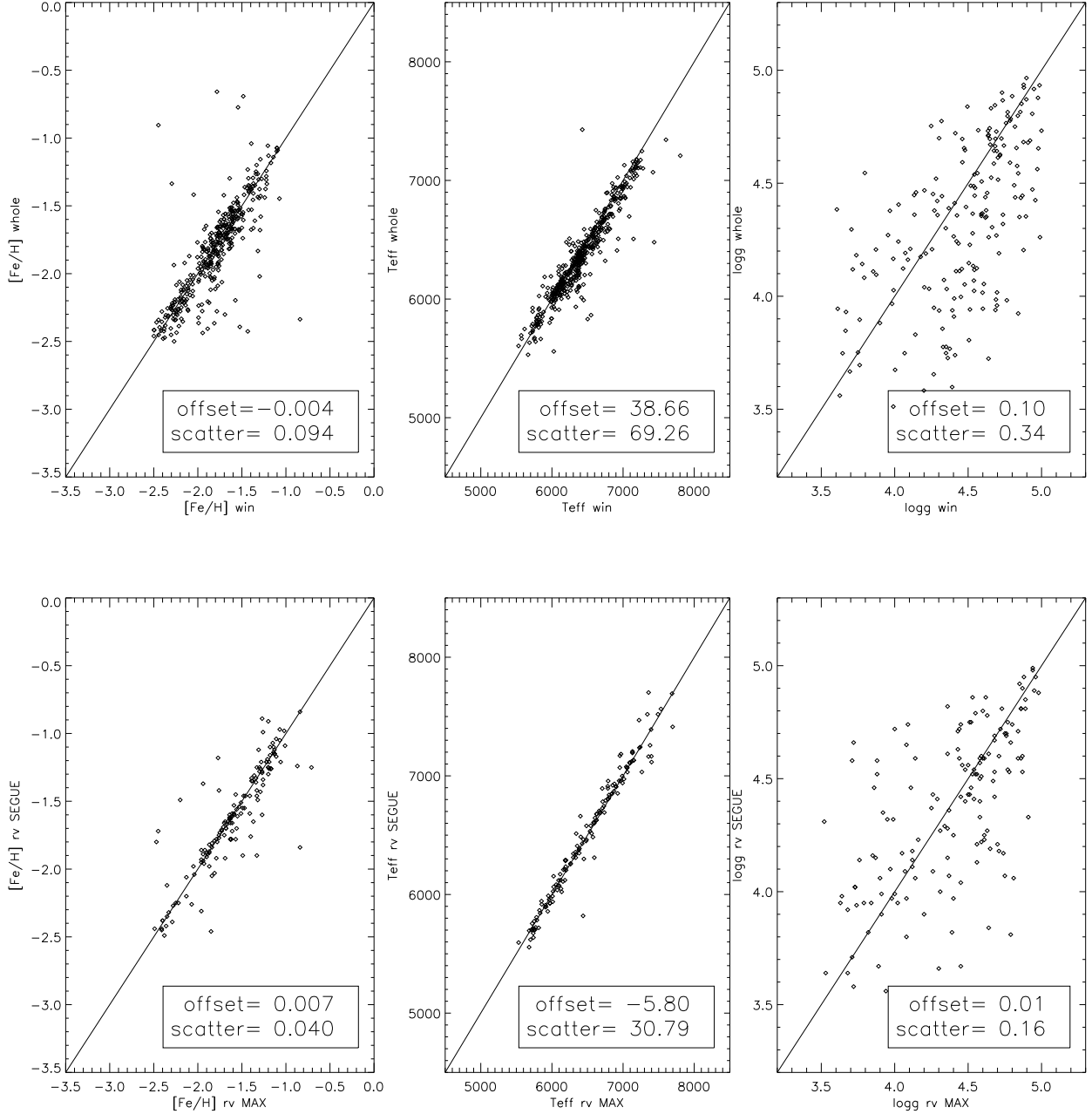


**Fig. 6.** Upper panel: Metallicity (left), effective temperature (middle) and surface gravity (right) obtained using MA $\chi$  for the entire spectral range of [3900, 5200] Å (whole) compared to the one with selected spectral windows (win) for a sample of 150 randomly selected stars. The offset (mean difference of “win - whole”) of the results and the scatter (standard deviation) of it is indicated at the bottom right of each plot. The line has a slope of unity. Lower panel: as upper panel but investigating the influence of using our radial velocities (rv MAX) or the SEGUE ones (rv SEGUE). Offset and scatters are calculated from the difference “SEGUE-MAX”.

#### 4.1. Whole domain vs. spectral windows

The classical  $\chi^2$  fitting procedure uses every datapoint; therefore, a straight-forward method to speed up the analysis would be to mask the parts of the spectrum which do not contain information about the parameters, essentially those that are merely continuum. Certainly, by considering only the CaII, Balmer and MgIb lines, we decrease the number of operations, increasing the processing speed of  $\chi^2$  calculations. This is clumsy however: an empirical decision must be made about the relevance of pixels,

and no extra weighting is considered - and the time taken for the parameters estimation is still large if one wants to do it for many spectra. The use of the **b**-vectors in the MA $\chi$  method means that very little weight is placed on pixels which do not change significantly with the parameter under study, automatically removing the sectors without lines.

The remarkable result of the MA $\chi$  method is that it is possible to determine the maximum of the compressed likelihood in 10 milliseconds using a present day standard desktop PC. This is at least 300 times faster than the same procedure when doing

an efficient evaluation of the uncompressed data.

The  $1\sigma$  confidence contours indicate errors in the parameters on average of 0.24 dex in metallicity, 130 K in temperature and 0.5 dex in gravity. Examples of fits are shown in Fig. 5. The upper plot shows the fit between a randomly selected SEGUE spectrum and the best model - the crosses correspond to the observed spectrum and the dashed red line to the model, with stellar atmosphere parameters in the legend, as well as the resulting reduced  $\chi^2$  of the fit. The plot in the bottom is the fit of the same star, but considering only the data points within the line regions identified in Table 1, as discussed above. Again, the red dashed line indicate the model with parameters in the legend. The  $\chi^2$  of the fit is also given.

Since the lines contain the most information about metallicity, temperature and gravity, we expect to obtain the same results whether we use all the data points or only those corresponding to the lines. The legends in Fig. 5 show the parameters estimated in both analyses. The small differences between them are within the  $1\sigma$  errors. We have plotted in the upper panel of Fig. 6 the comparison for metallicity (left panel), temperature (middle) and gravity (right) of our sample of stars when using the whole spectral range (“whole”) or only spectral windows with the lines (“win”). The offsets and scatters of the distribution are indicated on the legend of each plot, as well as the one-to-one relation. Here we have randomly selected 150 stars to plot in Fig. 6, in order to visualize better the correlations of the results. Offsets and scatters are calculated using the entire star sample. Metallicity has excellent agreements, with a small scatter of 0.094 dex, as shown in the legend of the plot. Temperature has a negligible offset of 38 K and a scatter of 69 K, which is also smaller than the accuracies obtained in the temperature estimation. Gravity has the largest scatter offset of 0.1 dex and a scatter of 0.34 dex, but this is still within the errors.

The negligible offsets obtained when using the entire spectral range against the limited regions is an encouraging result in terms of the effect of the G-Band in the spectrum. As pointed out above, the dependency of this feature in the parameters under study is not as strong as the rest of the lines of Table 1. This is translated into less weight for the compression, as seen in Fig. 1, meaning the G-band does not play a crucial role in our compressed data set for the parameter recovery.

Let us remark that this fact does not mean a lack of CEMP stars in our sample, we simply do not see them in the compressed space. A spectrum with a strong observed CH molecule gives a similar compressed  $\chi^2$  than one with a weak one, since the compression does not consider variations in carbon abundance. The full  $\chi^2$ , on the other hand, will certainly be larger for the spectrum with a strong G-band, because our models do not have different carbon abundances.

In any case, the fraction of CEMP stars is high and it is certainly interesting to locate them using the MA $\chi$  method in the future. This implies to create another dimension in the grid of synthetic spectra – models with varying carbon abundances – and increase the number of parameters to analyze by 5. One more dimension means certainly a heavier grid of models, but in terms of parameter recovery, there is no big difference to use 4 or 5  $y$ -numbers for the compressed  $\chi^2$  calculation. This study goes, however, beyond the purpose of this paper, where we are only introducing the MA $\chi$  method.

#### 4.2. Effect on radial velocities

As mentioned in Sect. 3.3 and seen in Fig. 4, radial velocities given by the SEGUE database have a mean difference of 20 km/s respect to ours. To study the effect of this difference in the final parameter estimation, we have analyzed a sub-sample of randomly selected 2,670 stars of our sample using SEGUE radial velocities. The comparison of the metallicity, effective temperature and surface gravity obtained when using our radial velocities (“rv MAX”) and the SEGUE ones (“rv SEGUE”) can be seen in the lower panel of Fig. 6. In this plot, also a small sample of randomly selected 150 stars was used in order to visualize better the results, but offsets and scatters are calculated considering the 2,670 stars. A difference in 20 km/s produces offsets and scatters in the three parameters, with  $0.007 \pm 0.040$  dex for metallicity,  $-5.08 \pm 30.79$  K for temperature and  $0.01 \pm 16$  dex for gravity. These offsets are negligible when compared with the  $1\sigma$  errors obtained the parameter estimation.

#### 4.3. Comparison with the SEGUE Stellar Parameter Pipeline

The SEGUE Stellar Parameter Pipeline (SSPP, Lee et al. 2008a,b; Allende Prieto et al. 2008) is a combination of different techniques to estimate the stellar parameters of SEGUE. Some of them are fitting the data to a grid of synthetic spectra as the k24 (Allende Prieto et al. 2006), and the k13, NGS1 and NGS2 ones (Lee et al. 2008a). Another method are the ANNSR and ANNRR of Re Fiorentin et al. (2007), which are an artificial neural network (ANN) trained using a grid of synthetic (S) or real (R) spectra in order to estimate the parameters of real spectra (R). Other options are line indices (Wilhelm et al. 1999) and the CaII K line index (Beers et al. 1999). We compare our results with the final adopted SSPP value (ADOP), and those of the k24, NGS1 and ANNSR grids of synthetic spectra. Each of these results can be found in the SSPP tables of the SDSS database. The grids of models are created using Kurucz stellar atmosphere models, but k24 and NGS1 cover the wavelength range of [4400,5500] Å. The ANNSR grid includes the CaII triplet close to 8600 Å.

Figure 7 shows the correlations between the results of these methods and our own ones. As in Fig. 6, we have plotted a random selection of 150 stars to visualize better the correlations, but values of offsets and scatters have made using the entire sample of 17,274 stars. The left panels correspond to the metallicity, the middle ones to temperature and the right ones to the surface gravity. The top row of plots shows the consist in a general comparison of all the different methods, plotted with different colors. The  $y$ -axis indicates the ADOP results and the  $x$ -axis the methods MA $\chi$  (black), NGS1 (blue), ANNSR (red) and k24 (green). The one-to-one line is also plotted in the figures. For each distribution a histogram of  $(\text{method}_i - \text{method}_j)$  with  $i \neq j$  was fitted with a gaussian to obtain estimations for offset (mean  $\Delta$ ) and scatter (standard deviation  $\sigma$ ). The results are summarized in Table 2. In the lower panel of Fig. 7 we have plotted the comparisons of individual methods for 150 stars randomly selected. These panels help to visualize better how the single methods of the pipeline and our own correlate with each other. Figure 7 and Table 2 show that our results are in reasonable agreement with the pipeline, and that the scatter is of the same order of magnitude as that between the individual SSPP methods.

Considering individual parameters, our metallicities have a general tendency to be  $\sim 0.3$  dex lower than adopted metallicity of SSPP (ADOP). A similarly large offset exists between ANNSR and NGS1, with  $-0.22$  dex. This could be due to the

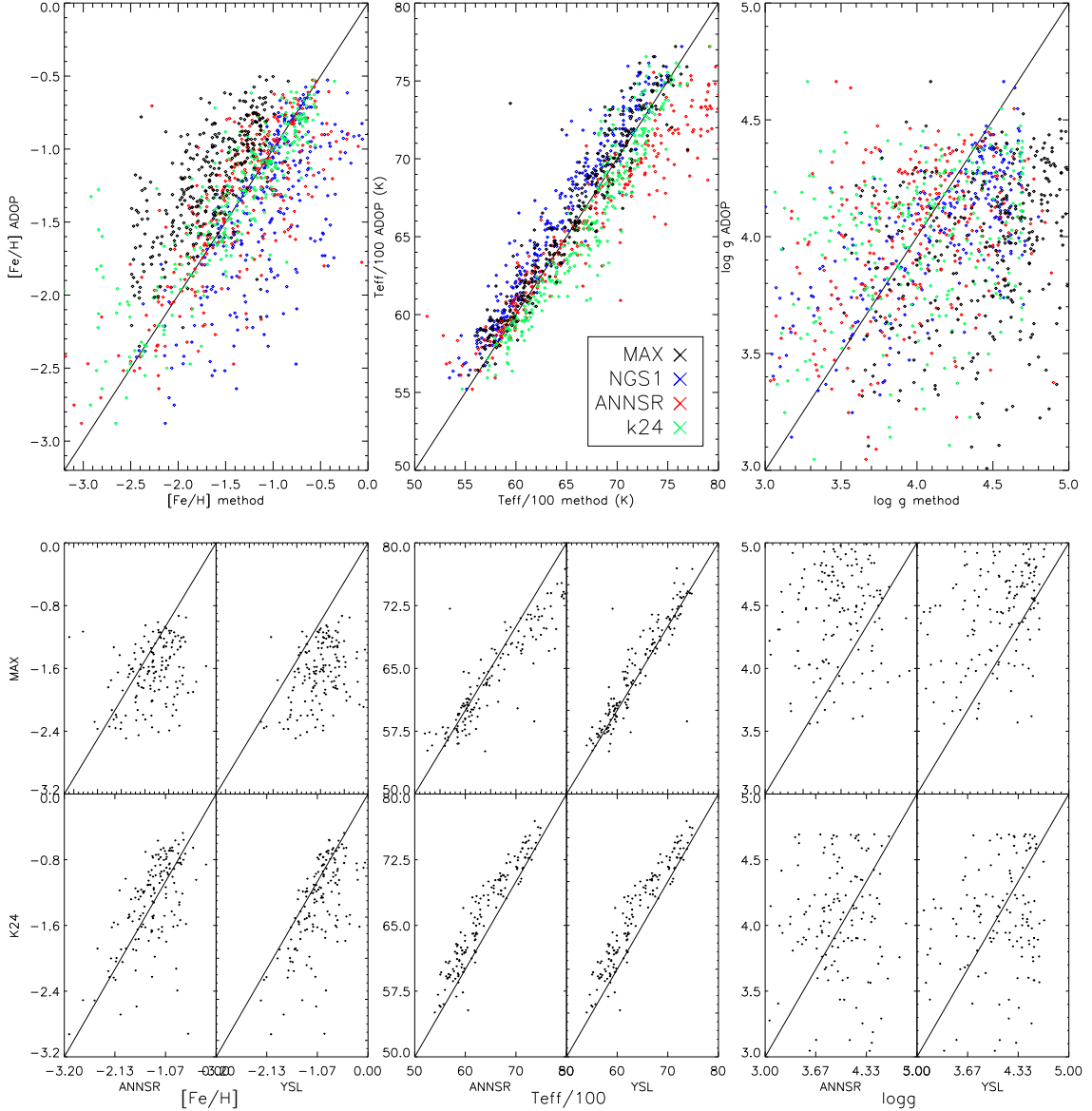


**Fig. 7.** Upper plot: Comparison of the results from the SEGUE Stellar Parameter Pipeline (SSPP) with different methods: This work (MAX, black), (Lee et al. 2008a, NGS1, blue), (Re Fiorentin et al. 2007, ANNSR, red) and (Allende Prieto et al. 2006, k24, green). Lower part: Comparisons of individual methods for a randomly selected subsample of stars. Each plot has a line with slope of unity. The different offsets and scatters between the results are indicated in Table 2. In each plot, a selection of 150 random stars has been used.

consideration of the CaII lines in the fit, which are not included in the NGS1 and k24 ones. ANNSR also includes CaII lines, the offset of  $-0.17$  dex to our results is smaller than  $1 \sigma$  error. In the case that the same lines are used in the fitting, no offset should be seen, as will be shown in Sect. 5.

The temperature, on the other side, shows a small offset of  $-61$  K with respect to the ADOP value of the pipeline. It is encouraging to see that we obtain the best agreement, except ANNSR, which has no offset. A large mean difference is found between k24 and NGS1, where the offset is  $244$  K. The scatter in the various comparisons varies from  $100$  K (NGS1 v/s ADOP) to  $200$  K (k24 v/s ANNSR); our scatter of  $112$  K with respect to ADOP is one of the smallest values.

Finally,  $\log g$  shows the largest offset. We derive gravity values  $0.51$  dex higher than the ADOP ones. The worst case is the comparison between our method and ANNSR with  $0.63$  dex. Between the methods of the pipeline, the largest difference ( $0.27$  dex) is found between ANNSR and NGS1. The best agreement we find in gravities are with NGS1, with an offset of  $0.38$  dex. The scatter for gravities varies from  $0.23$  dex (NGS1 v/s ADOP) to  $0.48$  dex (ANNSR v/s k24 and  $MA\chi$  v/s k24). A possible approach to correct our gravities would be to shift the zero point by  $-0.38$  dex to agree with those of NGS1. We prefer to accept that gravity is our least constrained parameter, given the lack of sensitive features except for the wings of the MgIb lines, and the noise in the spectra does not restrict  $\log g$  effectively. In order to deal with this problem, k24 and NGS1 smooth

the spectra to half of the resolution, gaining by this procedure signal-to-noise. We remark that the k24 grid includes g-r colors, also to constrain the temperature. This leads automatically to different gravity values. A more extensive discussion about this aspect will be presented in Sect. 5.6. The right panels of Fig. 7 shows that all  $\log g$  estimates are rather uncorrelated with each other with respect to the other ones.

#### 4.4. Systematic errors: Choice of fiducial model

The  $\mathbf{b}$ -vectors are basically derivatives with respect to the parameters. Under the assumption that the responses of the model to these derivatives are continuous, the choice of the fiducial model (FM) used to build the  $\mathbf{b}$ -vectors is free. This assumption, however, is only correct for certain regions of the parameter space. For example, Balmer lines are good temperature indicators for stars no hotter than 8000K (Gray 1992), and for cold stars spectral lines are affected by molecular lines. Limiting our candidate stars to the range of 5000K to 8000K we know that we have a clean spectra with Balmer lines as effective temperature indicators. This fact allows us to choose a FM with any temperature in that range to construct our weighting vector  $\mathbf{b}_{\text{Teff}}$ , which will represent well the dependency of the model spectrum on temperature. Similar assumptions are made for the other two model parameters.

In order to test this assumption we have studied the effect of using different fiducial models in the final results of the parameter estimation. In Fig. 8, we plot the results of metallicity (left), temperature (middle) and gravity (right) for 150 randomly selected SEGUE stars. There are four sets of different fiducial models [A,B] used for the  $\mathbf{b}$  vector calculation. The parameters of the FM are indicated at the right side in each set. From top to bottom, the first one compares results using a cold ( $T_{\text{eff}} = 5500$  K) and a hot ( $T_{\text{eff}} = 7500$  K) fiducial model of our grid of synthetic spectra, the second one a metal-poor ( $[\text{Fe}/\text{H}] = -2.0$ ) and a metal-rich ( $[\text{Fe}/\text{H}] = -0.8$ ) one. The third one considers two different gravities ( $\log g = 3.7$  and  $\log g = 4.7$ ). For these three sets, all other parameters are calculated identical. Finally, the last one uses models which vary all 3 parameters. The histograms of each plot correspond to the difference of the results obtained using the fiducial model with set of parameters A and B, respectively. The gaussian fit of the histogram is overplotted and its mean ( $\Delta$ ) and standard deviation ( $\sigma$ ) are indicated in the legend at the top.

Metallicity shows a well defined behavior under different  $\mathbf{b}$ -vectors. There are negligible offsets when varying only one parameter in the FM, except in the case where the FM is totally different. But even in that case, the offset of -0.15 dex is smaller than the  $1\sigma$  errors of 0.25 dex obtained in the metallicity estimation. We conclude that this parameter does not show real systematic offsets due to the choice of fiducial model. The scatter obtained in the metallicity is also smaller than the  $1\sigma$  errors of the results. Only in the last case (bottom left) it becomes comparable with the errors. Since gravity is a poorly constrained parameter (see discussions above) and the  $y$ -numbers are uncorrelated, the effect when using different gravities in the FM should be completely negligible in the result of the other parameters. This can be seen in the third panel from top to bottom of Fig. 8, where metallicity and temperature show extremely small offsets and scatters.

The derivation of temperature using different fiducial models shows a similar behaviour. The discrepancies between results

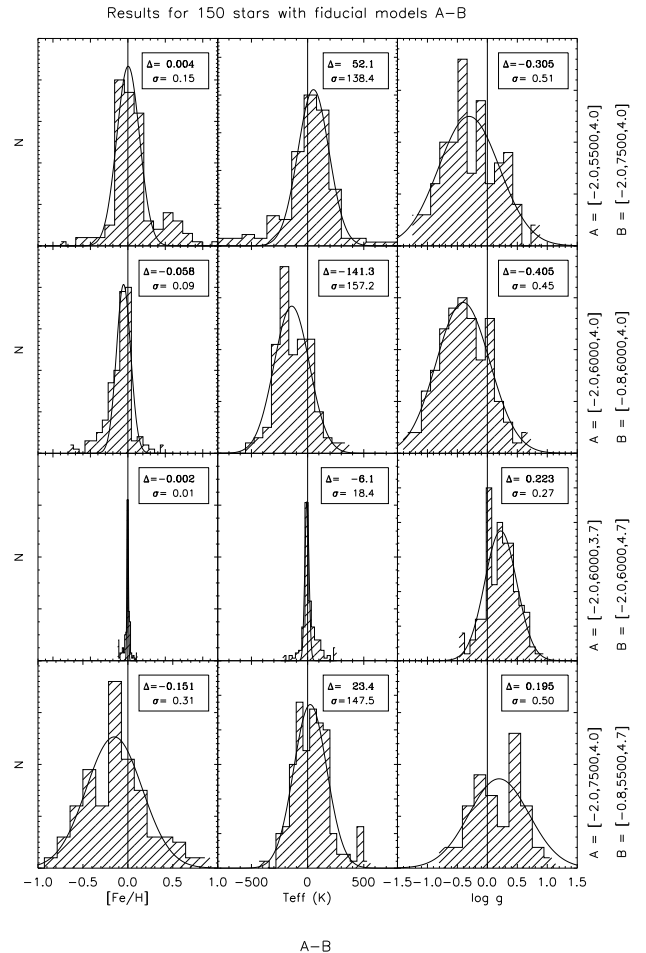


**Fig. 8.** Histograms of the differences of the results obtained using 8 different fiducial models for the compression. Left: metallicity, middle: temperature and right: gravity. The parameters of the fiducial model are indicated in the right side of each plot, labeled as  $[[\text{Fe}/\text{H}], T_{\text{eff}}, \log g]$ . Each histogram has a Gaussian fit, where the peak ( $\Delta$ ) and the standard deviation ( $\sigma$ ) are indicated in the top legend.

when using different FM are of the order of 50 K, except when the metallicity is varied. The mean difference of the final temperature estimates when using a metal-poor fiducial model and a metal-rich one is of 141 K, which is smaller than some differences seen in Table 2 between the methods of the SEGUE Stellar Parameter Pipeline. This happens probably because the spectrum of a metal-rich star presents more lines than a metal-poor one, which is translated into the  $\mathbf{b}$ -vector as temperature dependent regions that do not exist. In the case of SEGUE data, many of the weak lines seen in a metal-rich synthetic spectrum and(or) the  $\mathbf{b}$ -vector of a metal-rich fiducial model, are hidden by the noise in the observed spectra and the assumption of a temperature dependency due to these weak lines may not be correct. For the analysis of low signal-to-noise spectra, it is preferable to choose a FM with a rather low metallicity. But even when using a high metallicity for the FM, the offset is comparable with the  $1\sigma$  error of 150 K for the temperature estimations. We conclude that temperature neither shows a significant systematic offset due to choice of fiducial model.

**Table 2.** Offsets ( $\Delta$ ) and scatter ( $\sigma$ ) of the differences (row - column) between the methods: MA $\chi$  (this work), ADOP (Lee et al. 2008a), NGS1 (Lee et al. 2008a), ANNSR (Re Fiorentin et al. 2007) and k24 (Allende Prieto et al. 2006) for the entire sample of selected SEGUE stars.

	ADOP	NGS1	ANNSR	k24
	$\Delta/\sigma$	$\Delta/\sigma$	$\Delta/\sigma$	$\Delta/\sigma$
[Fe/H]				
MA $\chi$	-0.32 / 0.23	-0.41 / 0.29	-0.17 / 0.33	-0.34 / 0.26
k24	0.04 / 0.14	-0.07 / 0.25	0.17 / 0.27	
ANNSR	-0.13 / 0.22	-0.22 / 0.23		
NGS1	0.08 / 0.17			
T <sub>eff</sub>				
MA $\chi$	-61 / 112	80 / 132	-76 / 170	-159 / 160
k24	98 / 101	244 / 166	88 / 195	
ANNSR	1 / 114	147 / 173		
NGS1	-142 / 93			
log g				
MA $\chi$	0.51 / 0.39	0.38 / 0.43	0.63 / 0.47	0.41 / 0.48
k24	0.08 / 0.35	-0.02 / 0.42	0.26 / 0.48	
ANNSR	-0.14 / 0.36	-0.27 / 0.45		
NGS1	0.09 / 0.23			

Finally, gravity shows larger discrepancies in the final results when varying the FM. The differences can be in the worst case as large as 0.4 dex when using different metallicities in the FM. This could also be due to the fact that a metal-rich FM contains more lines and therefore, more sensitivities to gravity, which in our low signal-to-noise spectra is not the case. These sensitivities are confused with the noise in the observed spectrum. Scatters of 0.5 dex are in general of the order of the  $1\sigma$  errors.

## 5. Application to High Resolution Spectra

As a check, MA $\chi$  has also been tested with a smaller sample of 28 high resolution spectra. For consistency with the low resolution implementation, again metal-poor dwarf stars were selected.

### 5.1. Data

The spectra were obtained with UVES, the Ultraviolet Echelle Spectrograph (Dekker et al. 2000) at the ESO VLT 8 m Kueyen telescope, in Chile. The resolving power is  $R \sim 43,000$  and the signal-to-noise is typically above 300 in our spectra. Since MA $\chi$  is an automatic fitting tool for synthetic spectra, we first need to be sure that the observed spectra can be fitted by our grid of synthetic spectra. This means, we want to have easily distinguishable unblended spectral lines and a clear continuum. For these reasons, we have selected part of the red setting of the UVES spectra, which covers the wavelength range 580 nm - 680 nm, where there are many unblended lines.

### 5.2. Grid of high-resolution Models

When modeling spectra in high resolution, there are some differences to the low-resolution case and the following considerations have to be made:

- A value for microturbulence must be set, since the shape of strong lines depends sensitively on the value chosen for  $v_t$ . This is not the case in low resolution, such that there is no need to fine-tune this parameter. In high resolution the set of basic stellar atmosphere parameters is

([Fe/H], T<sub>eff</sub>, log g,  $v_t$ ). To do a proper parameter estimation we should create a 4-dimensional grid of synthetic spectra, varying all the parameters indicated above. This goes further than the purposes of this paper, where we want to check the applicability of our method. Therefore we fix the microturbulence parameter to a typical value, guided by the results of a standard “classical” spectral analysis (see below).

- To compute synthetic spectra, a list of lines with their wavelength and atomic data must be included. The atomic data consists of oscillator strength log  $gf$  and excitation potentials, which are an important source of differences in the final shape of a given line. For the comparison consistent line lists are needed.
- In order to make a proper fit to a large wavelength range, the models should be perfect. Our models are computed under the simplifying assumption of LTE and with plane-parallel atmosphere layers; the atomic data have errors, too. There are too many features to fit, therefore a global fit becomes difficult, almost impossible. For this reason we select windows of a limited spectral range, and fit the observed spectra only in these.

We determine the three parameters temperature, metallicity and gravity using neutral and ionized iron lines. Neutral lines are sensitive to temperature and single ionized ones to gravity (Fuhrmann 1998). The metallicity is effectively obtained from both FeI and II, for a given temperature and gravity. In the wavelength range of 580nm - 680nm, we have 6 FeII lines and 20 FeI ones that are unblended and strong enough to be present in most metal-poor stars of our sample. The lines are indicated in Table 3, where wavelength and log  $gf$  values are listed. The log  $gf$  values and excitation potentials are taken from Nissen et al. (2002) and the VALD database (Kupka et al. 2000).

Our grid of high resolution models covers a range in metallicity of  $-2.5 \leq [\text{Fe}/\text{H}] \leq -0.5$ , in effective temperature of  $5500 \leq T_{\text{eff}} \leq 6600$ , in surface gravity of  $3.5 \leq \log g \leq 5$  and in scaling factor for normalization from 0.85 to 1.15. The grid steps are the same as in Sect. 3.2. The models have  $[\alpha/\text{Fe}] = +0.4$  and  $v_t = 1.2$  km/s, according to the values obtained for our stars with the “classical” method (see below).

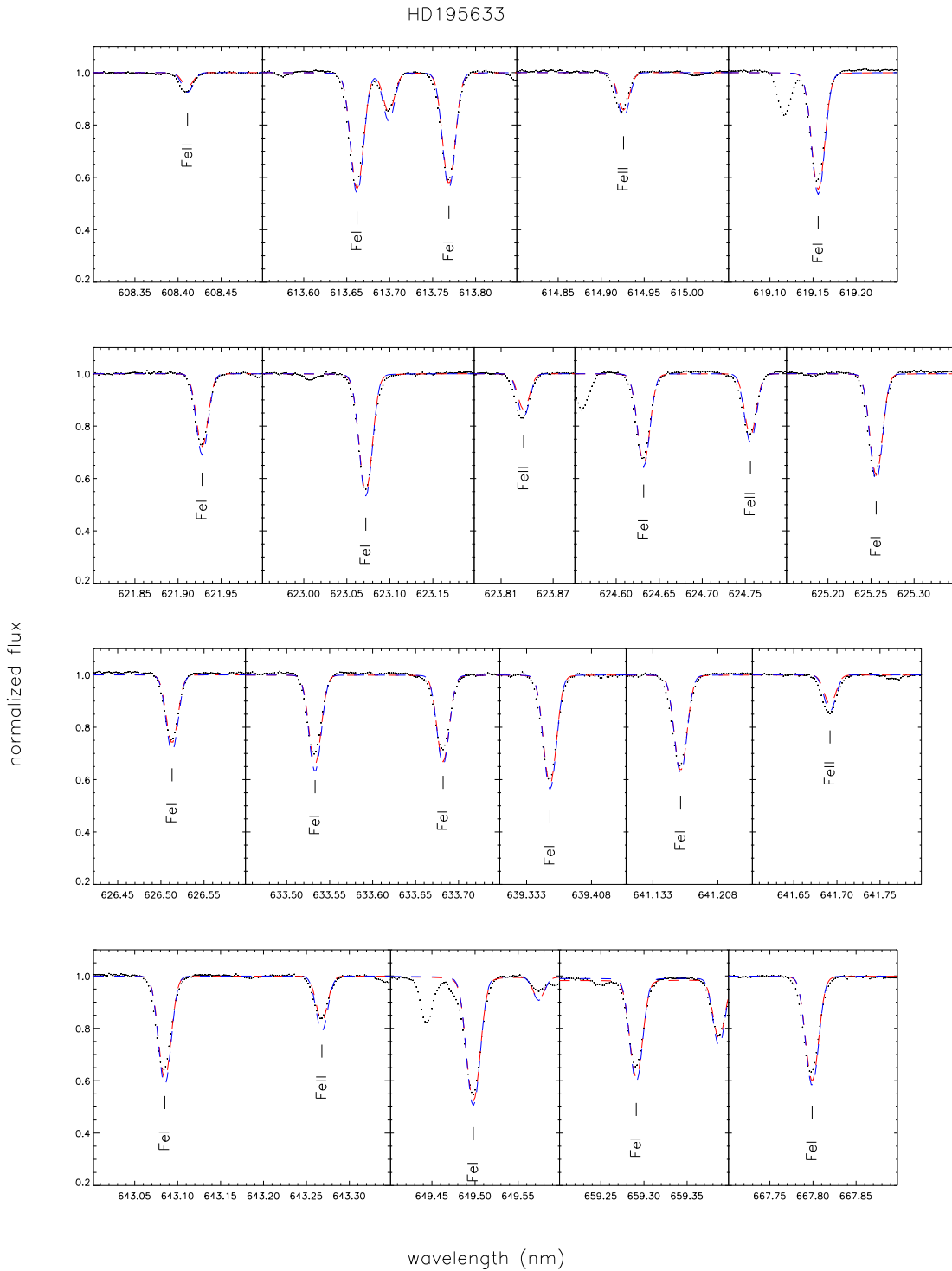


**Fig. 9.** Fit of the spectrum of the star HD195633 (points) with the best model (red dashed line). The parameters of the synthetic spectrum are  $[\text{Fe}/\text{H}] = -0.5$ ,  $T_{\text{eff}} = 6318$  K and  $\log g = 4.61$ , with  $\chi^2 = 6.31$ . Blue line correspond to the model with  $[\text{Fe}/\text{H}] = -0.6$ ,  $T_{\text{eff}} = 6005$  K and  $\log g = 3.86$  ( $\chi^2 = 7.31$ ), obtained using the “classical” approach. Each panel represents a spectral window where the lines from Table 3 are labeled at the bottom of them.

### 5.3. Preparing the observed data for synthetic spectral fitting

The reduction of the data is carried out in the same way as in Sect. 3.3, with the following difference in the normalization procedure. At this resolution, neither the polynomial fit-

ting approach by Allende Prieto et. al. (2006) nor IRAF<sup>6</sup> were able to find a good pseudo-continuum automatically. Hence,

<sup>6</sup> IRAF is distributed by the National Optical Observatory, which is operated by the Association of Universities of Research in Astronomy, Inc., under contract with the National Science Foundation.

**Table 3.** FeI and II lines used for the high-resolution fits. The first column indicates the wavelength; the  $\log gf$  value is taken from the VALD database and is given in the second column.

wavelength (Å)	$\log gf$
FeI	
6136.62	-1.410
6137.69	-1.403
6191.56	-1.416
6219.28	-2.448
6230.72	-1.281
6246.32	-0.877
6252.56	-1.767
6265.13	-2.540
6335.33	-2.177
6336.82	-0.856
6393.60	-1.576
6411.65	-0.717
6430.85	-1.946
6494.98	-1.239
6592.91	-1.473
6677.99	-1.418
FeII	
6084.11	-3.881
6149.26	-2.724
6238.39	-2.754
6247.56	-2.329
6416.92	-2.877
6432.68	-3.501

the observed spectra were normalized interactively using Midas (Crane & Banse 1982), and the synthetic spectra were computed with normalized flux. The compression procedure is the same as in Sect. 3.4. Compressing the grid of high resolution spectra takes more time than for the low resolution one, but this has to be carried out only once in order to obtain a new grid of  $y$ -numbers.

#### 5.4. Results of the high-resolution analysis using MA $\chi$

Figure 9 shows an example fit of HD195633 (points) with the best MA $\chi$  model (red dashed line) and the model with parameters found with the “classical” method (blue dashed line; see below). Each panel represents a spectral window with the lines of Table 3 used for the parameter estimation. All three parameters were determined simultaneously and the best fit corresponds to the model with parameters of  $[\text{Fe}/\text{H}] = -0.5$ ,  $T_{\text{eff}} = 6318$  K and  $\log g = 4.61$ . The final parameters of all stars in this sample are given in Table 4. The first column of the table indicates the name of the star and the 6 next ones are the parameters found with two different MA $\chi$  analyses. The first set (“free”) corresponds to the standard approach of determining all parameters simultaneously from the spectrum only. In the second variant (“restricted”) the gravity is determined independently using Eq. (14), which will be introduced in the following. The last 4 columns are the parameters obtained from the “classical” approach (below).

#### 5.5. Results of a “classical” analysis

In order to compare our MA $\chi$  results, we have analysed the spectra with a classical procedure, determining the stellar parameters through an iterative process. The method is basically the same as in, e.g., Nissen et al. (2002):

For the effective temperature it relies on the Infrared Flux Method, which provides the coefficients to convert colors to ef-

fective temperatures. We used the (V-K) color and the calibration of Alonso et al. (1996), after converting the K 2MASS filter (Skrutskie et al. 1997) to the Johnson filter (Bessell 2005) and de-reddening the color. The extinction was taken from Schlegel’s dust maps (Schlegel et al. 1998) in the few cases where we could not find the values in Nissen et al. (2002, 2004).

Surface gravities were determined using the basic parallax relation

$$\log g = \log \frac{M}{M_{\odot}} + \log \frac{T}{T_{\odot}} + 0.4 (Vc + BC) + 2 \log \pi + 0.12 + \log g_{\odot}, \quad (14)$$

where  $Vc$  is the  $V$  magnitude corrected for interstellar absorption,  $BC$  the bolometric correction and  $\pi$  the parallax in arcsec. We have adopted a different mass value for each star based on those of Nissen et al. (2002), which are between 0.7 and 1.1  $M_{\odot}$ . The bolometric correction  $BC$  was calculated using the solar calibration of  $BC_{\odot} = -0.12$  as in Nissen et al. (1997).

The equivalent widths of neutral and ionized iron lines are used to determine the metallicity  $[\text{Fe}/\text{H}]$ . It was obtained using Fitline (François et al. 2007), which fits Gaussians to the line profiles. The equivalent widths computed from these Gaussians fits were converted to abundances by running MOOG (Snedden 1973, Sobeck priv. comm. 2008) with the plane-parallel LTE MARCS model atmospheres of (Gustafsson et al. 2008), which differ from the ones used for MA $\chi$ . The line list contains the lines of Table 3 and more taken from bluer wavelengths in the range 300 - 580 nm (Hansen, priv. comm. 2009).

Finally, the value for the microturbulence was found by requiring that all the equivalent widths of neutral lines should give the same Fe abundance as the ionized lines.

In order to obtain the four parameters in this way, one starts with an initial guess for each one of the interdependent parameters. After determining them with the above steps all the values will change due to the interdependence, hence we have to iteratively apply the formulas until the parameters show a negligible change.

We are aware of the fact that our metallicity based on FeI lines is ignoring any non-LTE effects (Asplund 2005; Collet et al. 2005). But since neither the classically nor the MA $\chi$  analysis are taking this into account, the results obtained by both methods can well be compared.

The upper panels of Fig. 10 show the results of metallicity (left), temperature (middle) and gravity (right) for the entire sample of stars. The  $x$ -axis shows the results of the automatic fitting MA $\chi$  and the  $y$ -axis the “classical” parameter estimation (EW). The one-to-one line is overplotted in each figure and the legend indicates the mean of the differences (MA $\chi$  - EW) and its standard deviation, denoted as offset and scatter, respectively. Each point corresponds to a star of Table 4 with parameters obtained by the “free” method.

Gravity shows a scatter of  $\sigma = 0.46$  dex and a negligible offset. The determination of the gravity from FeII lines has always been a problematic task: Fuhrmann (1998), in an extensive study of parameters of nearby stars, showed that surface gravities of F-type stars located at the turn-off point, can easily differ by up to  $\sim 0.4$  dex if derived from either LTE iron ionization equilibrium or parallaxes. The amount of ionized lines (gravity dependent) present in the spectra is usually smaller than that of neutral ones (temperature dependent). By performing an automatic fitting of weighted spectra that contain only 6 FeII lines compared to 20 FeI lines, a scatter of 0.46 dex is reasonable.

The result for the effective temperature shows a very small offset of only  $-10$  K, but a quite large scatter of  $\sigma = 227$

**Table 4.** Parameters of the stars (column 1) obtained with MA $\chi$  for both types of analysis discussed in the text. In the first analysis all three parameters are determined using only the spectrum, while in the second one  $\log g$  was determined independently by using parallaxes according to Eq. (14), as for the case of the classical method (EW; last 4 columns)

star	MA $\chi$ , free			MA $\chi$ , restr.			classical, EW			$v_t$ (km/s)
	$T_{\text{eff}}$ (K)	$\log g$	[Fe/H]	$T_{\text{eff}}$ (K)	$\log g$	[Fe/H]	$T_{\text{eff}}$ (K)	$\log g$	[Fe/H]	
HD3567	6103.5	4.79	-1.200	6176.0	4.20	-1.223	6035.0	4.08	-1.200	1.50
HD19445	—	—	—	5746.5	4.10	-2.293	5982.0	4.38	-2.075	1.40
HD22879	5770.6	4.31	-0.877	5778.1	4.31	-0.880	5792.0	4.29	-0.885	1.20
HD25704	5638.9	3.61	-1.094	5864.4	4.19	-0.912	5700.0	4.18	-1.010	1.00
HD63077	5795.5	4.21	-0.796	5787.7	4.21	-0.793	5629.0	4.15	-0.935	0.90
HD63598	6078.6	4.79	-0.681	5804.1	4.23	-0.901	5680.0	4.16	-0.885	0.90
HD97320	5601.1	4.65	-1.411	6025.1	4.24	-1.183	6105.0	4.18	-1.175	1.20
HD103723	5999.2	4.29	-0.896	6004.4	4.29	-0.896	6128.0	4.28	-0.805	1.50
HD105004	5802.5	4.33	-0.900	5802.5	4.33	-0.900	5900.0	4.30	-0.800	1.10
HD106038	5994.6	4.48	-1.392	5995.5	4.48	-1.392	5950.0	4.33	-1.390	1.10
HD113679	6037.3	4.73	-0.500	5757.5	4.35	-0.708	5759.0	4.04	-0.590	0.90
HD116064	5757.7	4.58	-2.41	5757.7	4.58	-2.401	5999.0	4.33	-2.000	1.50
HD121004	5509.2	4.05	-0.670	5657.8	4.40	-0.650	5711.0	4.46	-0.725	0.65
HD122196	5811.8	3.50	-1.954	5810.2	3.56	-1.954	6048.0	3.89	-1.760	1.20
HD126681	5556.9	4.44	-1.055	5521.6	4.68	-1.075	5532.0	4.58	-1.170	0.60
HD160617	5804.1	3.50	-1.961	5985.2	3.75	-1.794	6028.0	3.79	-1.785	1.30
HD175179	6080.5	5.00	-0.500	5779.5	4.47	-0.691	5758.0	4.16	-0.690	0.90
HD188510	5568.8	4.35	-1.341	5500.0	4.65	-1.231	5536.0	4.63	-1.600	1.00
HD189558	5610.8	3.58	-1.191	5500.0	3.75	-1.181	5712.0	3.79	-1.145	1.20
HD195633	6318.2	4.61	-0.500	6037.7	3.99	-0.687	6005.0	3.86	-0.625	1.40
HD205650	5693.7	4.93	-1.195	5754.0	4.47	-1.208	5842.0	4.49	-1.170	0.90
HD298986	5891.5	3.66	-1.592	6297.9	4.22	-1.304	6144.0	4.18	-1.410	1.40
CD-333337	5808.2	3.66	-1.598	5946.9	3.85	-1.490	5952.0	3.95	-1.435	1.40
CD-453283	5500.0	4.26	-0.978	5885.5	5.00	-0.685	5657.0	4.97	-0.835	0.80
CD-571633	5939.9	4.37	-0.893	5939.9	4.37	-0.893	5907.0	4.26	-0.930	1.10
CD-3018140	6143.1	3.50	-2.095	6246.5	3.50	-1.980	6340.0	4.13	-1.870	1.00
G005-040	6228.2	5.00	-0.584	5930.4	4.52	-0.794	5766.0	4.23	-0.840	0.80
G013-009	6529.5	4.58	-2.29	6556.0	4.08	-2.299	6416.0	3.95	-2.225	1.40

K. Given the fact that two different methods were employed to determine it, this appears still to be acceptable. The scatter may also be affected by our fixed value for the microturbulence, which was taken from the average of the values found with the EW approach (see Table 4), but which in individual cases may differ severely.

One can decrease the scatter in the temperature difference by removing the three most discrepant objects from the sample. HD63598 (triangle) has an offset of 398 K. The Schlegel maps give a de-reddening for this star that is unrealistically large, so instead we have set it to zero. This leads to a temperature that is too low. Jonsell et al. (2005) have found a temperature of 5845 K for this star, reducing the difference to 233 K with respect to our result. G005-040 (asterisk) is the second case, where the offset is 462 K. For this star, the continuum subtraction was not perfect in all spectral windows, resulting in a fit where the parameters are quite unreliable. Finally, the weak lines of the observed spectrum of HD19445 pushed MA $\chi$  to the border of the grid. The parameters in this case were undetermined. By removing these three stars from our sample, the scatter for temperature is reduced to 197 K.

Metallicity, on the other hand, shows a very good agreement, with a negligible offset of 0.02 dex and a scatter of 0.16 dex (upper left panel of Fig. 10). The lines used for the automatic fitting (MA $\chi$ ) and for the classical analysis (EW) are in most cases identical, except for the lowest metallicities, where some of them are hardly visible. In such cases the classical method

resorted also to other lines outside the MA $\chi$  wavelength range. The atomic data are identical, but the value for microturbulence are not, as mentioned before. In view of all this, the very good correlation of metallicity is encouraging.

### 5.6. “Restricted” parameter recovery

An example for the individual fit of the best MA $\chi$  model to the observed spectra was shown in Fig. 9 for HD195633, which is shown as a filled symbol in Fig. 10 and is one of the objects with the largest discrepancies (see also Table 4). Nevertheless, the two synthetic spectra appear to fit equally well the observations ( $\chi^2 = 6.31$  for the MA $\chi$  model and  $\chi^2 = 7.31$  for the one obtained from the classical analysis). From the  $\chi^2$  values, we can not decide which method leads to a more accurate parameter determination for this star. One would need independent information of the spectrum about this star to reach conclusions about its parameters.

It is also interesting to notice from the upper panels of Fig. 10 that stars with large discrepancies in gravity (for example those with special symbols) give also large discrepancies in temperature, as expected. They show a quite unsatisfying fit for the FeII lines. Motivated by this, we did an additional test by restricting MA $\chi$  to the determination of the parameters using input values for  $\log g$  obtained from the EW method, i.e. we find a local maximum point of the likelihood in a restricted area. For doing this, we chose the 3 closest gravity values from our grid of synthetic

spectra to the classical one found with Eq. (14) – see column 9 of Table 4 – and we search for the maximum point within this range. May be that for  $\log g$  there is no local maximum in this range, and the final estimation will go to the border of the grid, as the case of CD-3018140, where  $\log g = 3.5$ . The general tendency is anyway the presence of a local maximum close to the input EW-value.

Now the agreement with the classical method for the effective temperatures becomes excellent, with a negligible offset of only 7.42 K and a scatter of 128 K, as seen in the lower panels of Fig. 10. Gravity gets also better constrained, with a small scatter of 0.14 dex and a negligible offset. Note that we do not necessarily obtain identical values, since the MA $\chi$  gravity is obtained by using the value from Eq. (14) only as input, and we are looking for a final solution close to this value. The behavior of metallicity does not change with respect to the “free” case, demonstrating the robustness of the determination of this parameter. The results obtained when using parallaxes for the initial guess for  $\log g$  are summarized in Table 4 in the columns under the heading “MA $\chi$ , restr.”.

It is instructive to discuss the implication of this comparison. In case of the “classical” EW method, we are determining the parameters making use of the best information available and of the freedom to adopt the method to each star individually. The iterative process allows us to decide where to stop the iteration, or, if no satisfying convergence can be reached, to draw on the options to move to another spectral window, to use other lines, or disregard problematic lines. Moreover, the continuum can be subtracted separately for each line, thus creating locally perfect normalized flux levels. For the effective temperature, the more reliable infrared flux method employing photometric data can be used instead of only relying on spectra. The advantage of determining  $\log g$  independently was already demonstrated.

On the other side, for our automatic MA $\chi$  method, we are attempting an estimation of the parameters only from the spectral information without fine-tuning the models or fit procedure for each star. Given this, the comparison with the full interactive method is surprisingly good. We demonstrated that by using additional information for one parameter (here  $\log g$ ) it becomes even better for the remaining two quantities. Table 4 shows our final parameter estimation for our stars, when we make use of the parallaxes as additional information.

The result of this test is that we demonstrated our ability to estimate the basic stellar atmosphere parameters quickly and accurately enough for a large sample of stars. While individually severe outliers may occur, overall, for a whole population of stars, the method is accurate. For such a purpose the EW method would be much too slow and tedious. Our method may also serve as a quick and rough estimate for a more detailed follow-up analysis.

## 6. Summary and Conclusions

We have described MA $\chi$ , a new derivative of MOPED for the estimation of parameters from stellar spectra. In this case the parameters were the metallicity, effective temperature and surface gravity. The method reduces the data to a compressed data set of 3 numbers, one per parameter. Assuming that the noise is independent of the parameters, the compressed data contains as much information about the parameters of the spectrum as the entire data itself. As a result, the likelihood surface around the peak is locally identical for the entire and compressed data sets, and the compression is ‘lossless’. This massive compression, with the degree of compression given by the ratio of the size of the data

to the number of parameters, allows the cost function calculation for a parameter set to be sped up by the same factor. In case of SDSS data, the spectra are of the order of 1000 datapoints, each with a corresponding error, that must be compared to a similarly sized model. The speed up factor in this case is then at least  $1000/3, \sim 333x$ .

This extremely fast multiple parameter estimation make the MA $\chi$  method a powerful tool for the analysis of large samples of stellar spectra. We have applied it to a sample of 17,274 metal-poor dwarf stars with low resolution spectra from SEGUE, using a grid of synthetic spectra with the parameter range of  $[-2.5, -0.5]$  dex in metallicity,  $[5000, 8000]$  K in effective temperature and  $[3.5, 5]$  dex in surface gravity, covering a wavelength range of  $[3850, 5200]$  Å.

From the CaII, Balmer and MgIb lines, which are the strongest absorption features identified in SDSS spectra, we estimated the metallicity with averaged accuracies of 0.24 dex, the temperature with 130 K and  $\log g$  with 0.5 dex, corresponding to the  $1\sigma$  errors. Surface gravity is a poorly constrained parameter using this data, mainly due to the lack of sensitive features to this parameter (apart from some degree of sensitivity of the wings of the MgIb triplet) and the large noise in the spectra when compared to high resolution spectra. Additional information to the spectra, such as photometry, would help to constrain more the gravity parameter.

MA $\chi$  has the option to fit simultaneously different spectral windows. We have compared estimates of the parameters using the whole spectrum and only those data ranges where known lines exist. Both analysis take approximately the same time, and give excellent agreement in recovered parameters. This suggests that for these low resolution spectra there is no need to carefully and laboriously select the spectral windows to be analyzed with MA $\chi$ , the method calculates this automatically as part of its weighting procedure.

Under the assumption that the spectra behave similarly under changes of the parameters, the choice of the fiducial model for the compression is free. We have created 8 compressed grids using different fiducial models for the  $\mathbf{b}$ -vector calculation and obtain agreement between the recovered parameters. Given the low signal-to-noise of our data, it is better to use a more metal-poor fiducial model, as the dependencies on the parameters will be focussed on the strong lines.

We have comprehensively investigated the correlations of our results with those obtained for the SEGUE Stellar Parameter Pipeline (Lee et al. 2008a), which reports results from a number of different methods. The results from MA $\chi$  give good agreement with those of the various pipelines, and any differences are consistent with those between the various accepted approaches. We are aware of the MATISSE (Recio-Blanco et al. 2006) method of parameter estimation, which uses a different combination of weighting data but is closer to the MA $\chi$  approach than the standard pipeline methods. We look forward to comparing our results with those of MATISSE when they become available.

More specifically, temperature shows an excellent agreement with the averaged temperature of SSPP, with a negligible offset of -61 K and low scatter of 112 K. Our metallicities show a tendency to be -0.32 dex lower than SSPP averages. The small scatter of 0.23 dex suggests that the different spectral features used in the analysis (mainly CaII lines) could shift the zero point of the metallicity. The largest discrepancy is found in surface gravity, where MA $\chi$  reports values 0.51 dex ( $\sigma = 0.39$ ) higher than the averaged value of the pipeline. We saw that this is consistent with the discrepancies seen between other methods.

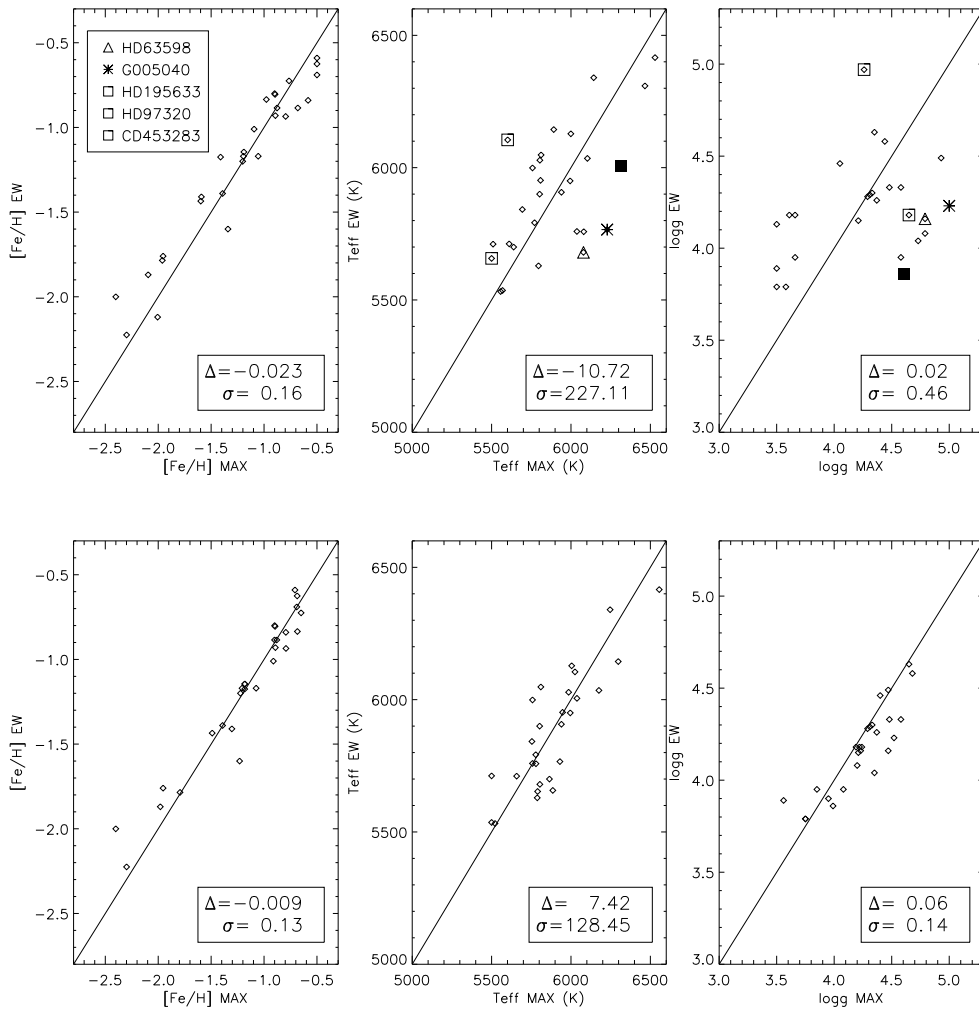


**Fig. 10.** Upper: Correlations between the results obtained using the automatic fitting (MAX) and the classical method (EW) for metallicity (left), temperature (middle) and gravity (right). In each panel, the one-to-one line is overplotted and a legend containing the mean difference (in the sense “EW-MA $\chi$ ”) and its standard deviation. Here the three parameters were determined simultaneously and directly from the spectra by our method. The stars with special symbols are indicated in the legend and correspond to special cases where the offset between the two methods is specially large (discussed in text). Lower: As upper panels, but MA $\chi$  results were obtained forcing the method to find the best fitting model close to the gravities computed from the parallax formula, Eq. (14). Individual data can be found in Table 4 (columns “MA $\chi$ , free” for the upper case and “MA $\chi$ , restr.” for the lower one)

We have also tested MA $\chi$  on a sample of 28 high resolution spectra from VLT-UVES, where no offset in metallicity is seen. In this case we have carefully chosen the models and spectral range for comparing our parameter estimation against a “classical” approach: temperature from photometry, surface gravity from parallaxes and metallicity from equivalent widths of neutral and ionized iron lines. We have calculated the parameters ourselves in order to avoid additional systematic offsets that various different methods would introduce in stellar parameter scales. These results were compared with the automatic fitting of 20 FeI and 6 FeII lines (that coincide in most of the cases with the equivalent widths calculations) made with MA $\chi$ . We obtained large scatter in gravity and temperature (0.44 dex and 220 K, respectively), but no systematic offset. The normalization of the continuum in some cases was not perfectly done, making it difficult to fit every line properly: especially in the case of the FeII lines. They produce a scatter in gravity, which drives a scatter in temperature.

We have seen in our fits that our best model does not differ very much from the model with parameters found by the “classical” approach. Motivated by this fact we decreased the scatter in gravity by using additional information to the spectrum, i.e. using the gravities determined from parallaxes as input value. This forces our method to find a local maximum point of the likelihood close to this input gravity value. Fixing the gravity gives an improved agreement in temperature, now with a scatter of 128 K. Metallicity does not change when forcing gravities, illustrating the robustness of determination for this parameter.

MA $\chi$  is an extremely rapid fitting technique, and as such is independent of model and data used. It will work for any star for which an appropriate grid of synthetic spectra can be calculated. Although the grid calculation is time consuming, it only needs to be performed once allowing extremely rapid processing of individual stars.

MA $\chi$  is one of the fastest approaches to parameter determination, and its accuracy is comparable with other methods. To de-

velop MA $\chi$  further in preparation for the next generation of surveys (eg. Gaia, APOGEE or LAMOST), we plan to expand our range of model grid and integrate photometric data to improve the determination of the parameters, especially surface gravity. We must be aware that in a grid of synthetic spectra with a broader parameter range, a set of **b**-vectors from one single fiducial model will not represent well the dependencies about the parameters in the entire sample. To cover the entire sample with well represented dependencies, we plan to compute different compressed grids, each of them with **b**-vectors calculated from different fiducial models. The parameter estimation in this case will be made with the different compressed grids using a final convergency test. After convergence, the final parameters should be estimated from the compressed grid with the fiducial model with parameters close to the final result.

*Acknowledgements.* This work is part of the PhD thesis of Paula Jofré and is funded by an IMPRS fellowship. We wish to thank Richard Gray, Martin Asplund, Francesca Primas and Jennifer Sobeck for their helpful comments in interpreting our results, Alan Heavens for algorithmic advice and especially Carlos Allende Prieto, for all the great advises and for sharing with the authors the continuum subtraction routine. P. Jofré is thankful to Timo Anguita and Manuel Aravena for programming tips and Thomas Mäder for his careful reading of the manuscript and the support to take this paper out. Finally, the authors gratefully acknowledge the many and detailed positive contributions made by the referee. Funding for the SDSS and SDSS-II has been provided by the Alfred P. Sloan Foundation, the Participating Institutions, the National Science Foundation, the U.S. Department of Energy, the National Aeronautics and Space Administration, the Japanese Monbukagakusho, the Max Planck Society, and the Higher Education Funding Council for England. The SDSS Web Site is <http://www.sdss.org/>.

The SDSS is managed by the Astrophysical Research Consortium for the Participating Institutions. The Participating Institutions are the American Museum of Natural History, Astrophysical Institute Potsdam, University of Basel, University of Cambridge, Case Western Reserve University, University of Chicago, Drexel University, Fermilab, the Institute for Advanced Study, the Japan Participation Group, Johns Hopkins University, the Joint Institute for Nuclear Astrophysics, the Kavli Institute for Particle Astrophysics and Cosmology, the Korean Scientist Group, the Chinese Academy of Sciences (LAMOST), Los Alamos National Laboratory, the Max-Planck-Institute for Astronomy (MPIA), the Max-Planck-Institute for Astrophysics (MPA), New Mexico State University, Ohio State University, University of Pittsburgh, University of Portsmouth, Princeton University, the United States Naval Observatory, and the University of Washington.

## References

- Abazajian et al., K. N. 2009, *ApJS*, 182, 543  
 Allende Prieto, C., Sivarani, T., Beers, T. C., et al. 2008, *AJ*, 136, 2070  
 Allende Prieto et al., C. 2006, *ApJ*, 636, 804  
 Alonso, A., Arribas, S., & Martínez-Roger, C. 1996, *A&A*, 313, 873  
 Asplund, M. 2005, *ARA&A*, 43, 481  
 Ballot, J., García, R. A., & Lambert, P. 2006, *MNRAS*, 369, 1281  
 Beers, T. C., Chiba, M., Yoshii, Y., et al. 2000, *AJ*, 119, 2866  
 Beers, T. C., Preston, G. W., & Shectman, S. A. 1992, *AJ*, 103, 1987  
 Beers, T. C., Rossi, S., Norris, J. E., Ryan, S. G., & Shefler, T. 1999, *AJ*, 117, 981  
 Bessell, M. S. 2005, *ARA&A*, 43, 293  
 Bond, J. R., Jaffe, A. H., & Knox, L. 1998, *Phys. Rev. D*, 57, 2117  
 Bond, N. A., Ivezić, Z., Sesar, B., Juric, M., & Munn, J. 2009, *ArXiv e-prints*  
 Castelli, F. & Kurucz, R. L. 2003, in *IAU Symposium*, Vol. 210, *Modelling of Stellar Atmospheres*, ed. N. Piskunov, W. W. Weiss, & D. F. Gray, 20P–+  
 Collet, R., Asplund, M., & Thévenin, F. 2005, *A&A*, 442, 643  
 Crane, P. & Banse, K. 1982, *Memorie della Societa Astronomica Italiana*, 53, 19  
 Dekker, H., D’Odorico, S., Kaufer, A., Delabre, B., & Kotzłowski, H. 2000, in *Society of Photo-Optical Instrumentation Engineers (SPIE) Conference Series*, Vol. 4008, *Society of Photo-Optical Instrumentation Engineers (SPIE) Conference Series*, ed. M. Iye & A. F. Moorwood, 534–545  
 François, P., Depagne, E., Hill, V., et al. 2007, *A&A*, 476, 935  
 Fuhrmann, K. 1998, *A&A*, 338, 161  
 Fukugita, M., Ichikawa, T., Gunn, J. E., et al. 1996, *AJ*, 111, 1748  
 Gray, D. F. 1992, *The observation and analysis of stellar photospheres.*, ed. D. F. Gray  
 Gray, R. O. & Corbally, C. J. 1994, *AJ*, 107, 742  
 Gray, R. O., Graham, P. W., & Hoyt, S. R. 2001, *AJ*, 121, 2159  
 Grevesse, N. & Sauval, A. J. 1998, *Space Science Reviews*, 85, 161  
 Gustafsson, B., Edvardsson, B., Eriksson, K., et al. 2008, *A&A*, 486, 951  
 Heavens, A. F., Jimenez, R., & Lahav, O. 2000, *MNRAS*, 317, 965  
 Ivezić, Z., Sesar, B., Juric, M., et al. 2008, *ApJ*, 684, 287  
 Jonsell, K., Edvardsson, B., Gustafsson, B., et al. 2005, *A&A*, 440, 321  
 Juric, M., Ivezić, Z., Brooks, A., et al. 2008, *ApJ*, 673, 864  
 Kupka, F. G., Ryabchikova, T. A., Piskunov, N. E., Stempels, H. C., & Weiss, W. W. 2000, *Baltic Astronomy*, 9, 590  
 Kurucz, R. L. 1992, *Revista Mexicana de Astronomia y Astrofisica*, vol. 23, 23, 45  
 Lee, Y. S., Beers, T. C., Sivarani, T., et al. 2008a, *AJ*, 136, 2022  
 Lee, Y. S., Beers, T. C., Sivarani, T., et al. 2008b, *AJ*, 136, 2050  
 Lucatello, S., Beers, T. C., Christlieb, N., et al. 2006, *ApJ*, 652, L37  
 Marsteller, B., Beers, T. C., Thirupathi, S., et al. 2009, *AJ*, 138, 533  
 Nelder, J. A. & Mead, R. 1965, *Comput. J.*, 7, 308  
 Nissen, P. E., Chen, Y. Q., Asplund, M., & Pettini, M. 2004, *A&A*, 415, 993  
 Nissen, P. E., Hoeg, E., & Schuster, W. J. 1997, in *ESA Special Publication*, Vol. 402, *Hipparcos - Venice '97*, 225–230  
 Nissen, P. E., Primas, F., Asplund, M., & Lambert, D. L. 2002, *A&A*, 390, 235  
 Nordström, B., Mayor, M., Andersen, J., et al. 2004, *A&A*, 418, 989  
 Panter, B., Heavens, A. F., & Jimenez, R. 2003, *MNRAS*, 343, 1145  
 Perryman, M. A. C., de Boer, K. S., Gilmore, G., et al. 2001, *A&A*, 369, 339  
 Press, W. H. 1993, *Science*, 259, 1931  
 Prugniel, P., Soubiran, C., Koleva, M., & Le Borgne, D. 2007, *ArXiv Astrophysics e-prints*  
 Re Fiorentin, P., Bailer-Jones, C. A. L., Lee, Y. S., et al. 2007, *A&A*, 467, 1373  
 Recio-Blanco, A., Bijaoui, A., & de Laverny, P. 2006, *MNRAS*, 370, 141  
 Rockosi, C., Beers, T. C., Majewski, S., Schiavon, R., & Eisenstein, D. 2009, in *Astronomy*, Vol. 2010, *AGB Stars and Related Phenomena 2010: The Astronomy and Astrophysics Decadal Survey*, 14–+  
 Schlegel, D. J., Finkbeiner, D. P., & Davis, M. 1998, *ApJ*, 500, 525  
 Skrutskie, M. F., Schneider, S. E., Stiening, R., et al. 1997, in *Astrophysics and Space Science Library*, Vol. 210, *The Impact of Large Scale Near-IR Sky Surveys*, ed. F. Garzon, N. Epchtein, A. Omont, B. Burton, & P. Persi, 25–+  
 Sneden, C. A. 1973, PhD thesis, AA(THE UNIVERSITY OF TEXAS AT AUSTIN.)  
 Snider, S., Allende Prieto, C., von Hippel, T., et al. 2001, *ApJ*, 562, 528  
 Steinmetz, M., Zwitter, T., Siebert, A., et al. 2006, *AJ*, 132, 1645  
 Tegmark, M., Taylor, A. N., & Heavens, A. F. 1997, *ApJ*, 480, 22  
 Thakur, A., Szalay, A. S., & Gray, J. 2004, in *Astronomical Society of the Pacific Conference Series*, Vol. 314, *Astronomical Data Analysis Software and Systems (ADASS) XIII*, ed. F. Ochsenbein, M. G. Allen, & D. Egret, 38–+  
 Tojeiro, R., Heavens, A. F., Jimenez, R., & Panter, B. 2007, *MNRAS*, 381, 1252  
 Wilhelm, R., Beers, T. C., & Gray, R. O. 1999, *AJ*, 117, 2308  
 Wyse, R. F. G. 2006, *Memorie della Societa Astronomica Italiana*, 77, 1036  
 Yanny, B., Rockosi, C., Newberg, H. J., et al. 2009, *AJ*, 137, 4377  
 York et al., D. G. 2000, *AJ*, 120, 1579  
 Zhao, G., Chen, Y., Shi, J., et al. 2006, *Chinese Journal of Astronomy and Astrophysics*, 6, 265